

Comparisons of the Aerodynamic Performance of two Silver Arrows from the Thirties

-An Analysis with Computational Fluid Dynamics

Bachelor Thesis in Applied Mechanics

JOHAN BONDESSON
HENRIK FORSTING
TIM GYNNING OLOFSSON
GABRIELLA HJÄLT
GUSTAV MARKSTRÖM
ERIK SJÖSVÄRD

Department of Applied Mechanics
Division of Vehicle Engineering and Autonomous Systems
CHALMERS UNIVERSITY OF TECHNOLOGY
Gothenburg, Sweden 2014
Bachelor Thesis nr 2014:02

BACHELOR THESIS 2014:02

Comparisons of the Aerodynamic Performance of two Silver Arrows from the Thirties

Bachelor Thesis in Applied Mechanics

JOHAN BONDESSON
HENRIK FORSTING
TIM GYNNING OLOFSSON
GABRIELLA HJÄLT
GUSTAV MARKSTRÖM
ERIK SJÖSVÄRD

Department of Applied Mechanics
Division of Vehicle Engineering and Autonomous Systems
CHALMERS UNIVERSITY OF TECHNOLOGY
Gothenburg, Sweden 2014

Comparisons of the Aerodynamic Performance of two Silver Arrows from the Thirties
Bachelor Thesis in Applied Mechanics

JOHAN BONDESSON
HENRIK FORSTING
TIM GYNNING OLOFSSON
GABRIELLA HJÄLT
GUSTAV MARKSTRÖM
ERIK SJÖSVÄRD

© JOHAN BONDESSON, HENRIK FORSTING, TIM GYNNING OLOFSSON, GABRIELLA HJÄLT, GUSTAV
MARKSTRÖM, ERIK SJÖSVÄRD, 2014

Bachelor thesis nr 2014:02
ISSN 1654-4676
Division of Vehicle Engineering and Autonomous Systems
Chalmers University of Technology
SE-412 96 Gothenburg
Sweden
Telephone: + 46 (0)31-772 1000

Cover: Velocity streamlines on the Mercedes-Benz W25 and the Auto Union Type C on the Monaco
race track. (Warter, 2011)

Department of Applied Mechanics
Gothenburg, Sweden 2014

Abstract

In the 1930's, the motor sport was dominated by the German manufacturers Auto Union (today Audi) and Mercedes-Benz. Their unique cars, known as *the Silver Arrows* due to their visible surface of aluminium, were then by far the most outstanding race cars at the Grand Prix. Their cutting edge technology provided great striking power and even today, engineers are astonished by their feat of engineering.

A Bachelor thesis from 2013 was carried out to model and to simulate two Silver Arrows (Auto Union Type C and Mercedes-Benz W25) in a commercial CFD software. At the time, previous CAD data were not available for the cars, thus the models were created from scratch using two CMC models in scale 1:18. The thesis reports that the large time consumption required for the CAD modelling accompanied that the work of the simulations could not be performed as desired.

The purpose of the 2014 thesis was to improve the existing flow analysis of the Silver Arrows. It was done by improving the above mentioned CAD models and to execute new, more reliable simulations of these; at different speeds and angles of the cars.

This project is based on a standard procedure for any CFD process; with a three-module workflow. The initial stage was *pre-processing*, where the previous year's CAD models were refined in CATIA V5. For instance, both engine blocks and parts on the cars surfaces were modified to create two more realistic models of the Silver Arrows. The complete CAD models were then processed in ANSA where a surface mesh was generated and then imported into STAR-CCM+. In STAR-CCM+ a virtual wind tunnel was created and a full volume mesh was generated.

The second stage was *solving* in STAR-CCM+ by performing a number of simulations. A total of 23 simulations were completed with different angles and different velocities of the cars.

In the final and third stage, the *post-processing* was performed by analysing and visualizing the results of the completed simulations. By creating a number of different scenes per simulation, the changes in pressure and velocity among others could be visualized.

The simulations show that the Silver Arrows are relatively well designed in an aerodynamic perspective, which mainly applies to the Mercedes-Benz W25. The Auto Union Type C has a much higher drag force in comparison. The cars exhibit none or almost no negative lift force, which can be expected, considered as knowledge about its significance was minor. The conclusion is that the Mercedes-Benz W25 is better designed in an aerodynamic perspective regardless of angles or speed of the cars.

Overall, the project has proceeded according to plan. Out of the 24 simulations that were wished to conduct, 23 received reliable results. In essence, all objectives have been answered.

Sammanfattning

Racingsporten under 1930-talet dominerades av de tyska biltillverkarna Auto Union (nutidens Audi) och Mercedes-Benz. Deras unika bilar som har blivit ihågkomna som Silverpilarna, på grund av deras exponerade yta av aluminium, var då de mest överlägsna på Grand Prix-tävlingarna. Den banbrytande teknik som dåtidens ingenjörer använde hade stor slagkraft och än idag är ingenjörer fascinerade av deras ingenjörskonst.

År 2013 gjordes ett kandidatarbete med utgångspunkt att virtuellt modellera samt aerodynamiskt simulera i kommersiellt CFD-program två stycken av dessa Silverpilar (Auto Union Typ C och Mercedes-Benz W25). Någon tidigare CAD-data för bilarna fanns inte att tillgå, således fick modellernas skapas från grunden med hjälp av två stycken CMC-modeller i skala 1:18. Den stora tidsåtgång som krävdes för modelleringen av CMC-modellerna medförde att arbetet med simuleringarna inte kunde utföras enligt önskemål.

Syftet med årets kandidatarbete var att förbättra den befintliga flödesanalysen av Silverpilarna. Detta gjordes genom att förbättra föregående års CAD-modeller samt utföra nya mer tillförlitliga simuleringar på dessa i olika hastigheter och vinklar.

Detta projekt utgick från ett standardiserat arbetssätt för CFD-processer genom ett arbetsflöde med tre olika delmoment. I det inledande skedet gjordes *förbehandlingen* genom att föregående års CAD-modeller förfinades i CATIA V5. Bland annat omarbetades förra årets motorblock samt delar på bilarnas ytor för att skapa två mer realistiska modeller av Silverpilarna. De färdiga CAD-modellerna bearbetades sedan i ANSA där ett ytnät generades för att sedan importeras in i STAR-CCM+. I det sistnämnda programmet skapades en virtuell vindtunnel innehållande ett fullständigt volymnät.

I det andra skedet gjordes *problemlösningen* i STAR-CCM+ genom att utföra ett antal olika simuleringar av Silverpilarna. Sammanlagt gjordes 23 simuleringar där olika vinklar på bilarna samt olika hastigheter testades för att så goda slutsatser som möjligt kring de aerodynamiska egenskaperna hos bilarna skulle kunna dras.

I det avslutande och tredje skedet gjordes *efterbehandlingen*, vilken utfördes genom att analysera och visualisera resultatet från tidigare gjorda simuleringar. Genom att skapa ett antal olika scener per simulering åskådliggjordes bland annat hur tryck samt hastighet förändrades över ytan.

Simuleringarna visar att dåtidens Silverpilar är relativt välformade ur ett aerodynamiskt perspektiv. Detta gäller främst Mercedes-Benz W25 som i jämförelse med Auto Union Typ C har ett betydligt lägre strömningsmotstånd. Bilarna påvisar ingen eller näst intill ingen negativ lyftkraft vilket kan anses väntat då kunskap kring betydelsen då var liten. Slutsatsen som drogs är att Mercedes-Benz W25 är bättre utformad ur ett aerodynamiskt perspektiv oavsett vinkel eller hastighet på bilen.

Sammantaget har projektet fortlöpt i stort sätt enligt planering. Av de 24 simuleringar som önskades genomföras har 23 fått tillförlitliga resultat. I enlighet med uppsatta målformuleringar har samtliga kunnat besvaras under projektets gång.

Preface

This report presents the final results of a bachelor thesis carried out during the period 2014-01-27 to 2014-06-02 at the Department of Applied Mechanics at Chalmers University of Technology, Gothenburg Sweden. The objective of this report was, with the base from the previous year's project, to analyse the aerodynamic properties of two Silver Arrows from the 1930s.

Based on last year's project some refinements were done with the CAD models to ensure closer similarity to the CMC models. Analyses of the aerodynamic properties were then carried out in the commercial software STAR-CCM+ where the cars were simulated with varying angles and velocities.

Readers are recommended to have basic knowledge of fluid dynamics and CFD.

Acknowledgments

First we would like to thank our supervisor, Ph.D. student Teddy Hobeika for his impeccable assistance throughout the whole project. Thank you for dedicating your time, patience and helpfulness during all the steps of this project.

Then we would like to thank Prof. Lennart Löfdahl for the opportunity to be a part of this project. Thank you for your immense interest and expertise for this subject, it has inspired us throughout the project.

Last but not least, we would like to thank the writers of the bachelor thesis from 2013 for their work that has been a good foundation for ours.

Nomenclature

CAD	Computer Aided Design
CFD	Computational Fluid Dynamics
CMC model	Classic Model Car
PID	Part Identity
RANS	Reynolds Averaged Navier-Stokes equation
Separation	The detachment of a boundary layer from a surface into a broader wake
Streamlines	The curve to which the velocity vector is tangent in every point
Wake	The region of recirculating flow immediately behind a moving or stationary solid body
A_0	Model constant in the $k - \varepsilon$ model: 4,04
A_p	Projected frontal area
A_s	Model constant in the $k - \varepsilon$ model: $\sqrt{6} \cos(\phi)$
a	Speed of sound, for air in standard condition: 340,29m/s
C	Inertial resistance
C_D	Drag coefficient
C_L	Lift coefficient
C_f	Skin friction coefficient
C_p	Pressure coefficient
C_1	$\max \left[0,43; \frac{\eta}{\eta+5} \right]$
C_{1e}	Constant: 1,44
C_2	Constant: 1,9
$C_{3\varepsilon}$	Model constant: -0,33
C_μ	Turbulent viscosity constant in the $k - \varepsilon$ model
C^+	Constant $\approx 5,0$
E	Energy

E_k	Empirical constant: 9,793
e	dE/dm
F	Force
F_{Drag}	Drag force
F_{Lift}	Lift force
$F_{Lift Front}$	Lift force on the front axle
$F_{Lift Rear}$	Lift force on the rear axle
k	Turbulent kinetic energy
L	Length
\ln	The natural logarithm
Ma	Mach number, a dimensionless number based on the relation between the velocity of the fluid and the speed of sound of a perfect gas
m	Mass
\mathbf{n}	Normal vector
P	Pressure
\bar{p}	Time averaged pressure
\acute{p}	Fluctuating pressure
p	Static pressure
p_∞	Free stream pressure
P_b	Generation of turbulence kinetic energy due to buoyancy
P_k	Generation of turbulence kinetic energy due to the mean velocity gradients
P_0	Stagnation pressure, highest possible pressure in the flow obtained when the velocity approaches zero
Re	Reynolds number, a dimensionless quantity that helps predict similar flow patterns for different fluid flows
S	Constant: $\sqrt{2S_{ij}S_{ij}}$
S_{ij}	Strain rate of the mean flow

S_k	User-defined source terms
$\widetilde{S^3}$	Normalized mean rate of strain tensor: $\sqrt{S_{ij}S_{ij}}$
S_ε	User-defined source terms
T	Time
t_0	Start time
U	Velocity vector
U_p	Mean velocity
U^*	Model for the fluid-particle velocity
u	Velocity in x-direction
u_τ	Friction velocity or shear velocity
\bar{u}	Time averaged velocity in x-direction
\acute{u}	Fluctuating velocity in x-direction
u^+	Dimensionless velocity parallel to the wall as a function of y^+
V	Volume
\mathbf{V}	Velocity vector
\mathbf{V}_r	Relative velocity
v	Velocity in y-direction
\bar{v}	Time averaged velocity in y-direction
\acute{v}	Fluctuating velocity in y-direction
W	Angle: $\frac{S_{ij}S_{jk}S_{ki}}{\widetilde{S^3}}$
w	Velocity in z-direction
\bar{w}	Time averaged velocity in z-direction
\acute{w}	Fluctuating velocity in z-direction
Y_M	Contribution of the fluctuating dilation
y_0	Distance from the boundary at which the idealized velocity given by the law of the wall goes to zero
y_p	Distance from the wall

y^+	Dimensionless distance to the wall
y_v^+	Constant: 11,225
α	Viscous resistance
β	dB/dm
ε	Turbulent kinetic energy dissipation rate
δ_{ij}	Kronecker delta
η	Fluid viscosity: $S \frac{k}{\varepsilon}$
θ	Angle
κ	Von Kármán's constant: 0,4187
μ	Dynamic viscosity
μ_t	Eddy viscosity
ν	Kinetic viscosity
ρ	Density
τ_{wall}	Wall shear stress
σ_k	Turbulent Prandtl number for k , constant: 1,0
σ_ε	Turbulent Prandtl number for ε , constant: 1,2
τ_{ij}	Stress tensor
ϕ	Angle: $\frac{1}{3} \cos^{-1}(\sqrt{6}W)$
$\overline{\Omega}_{ij}$	Anti symmetric rate-of-rotation tensor viewed in a rotating reference frame
$\tilde{\Omega}_{ij}$	Mean-rate of rotation tensor: $\overline{\Omega}_{ij} - 3\varepsilon_{ijk}\omega_k$
Ω_{ij}	Rate of rotation tensor
ω_k	Angular velocity

Table of Contents

ABSTRACT	I
SAMMANFATTNING	III
PREFACE	V
ACKNOWLEDGMENTS	V
NOMENCLATURE	VI
TABLE OF CONTENTS	X
1. INTRODUCTION	1
1.1. OBJECTIVE.....	2
1.2. LIMITATIONS	2
2. HISTORICAL BACKGROUND	3
3. BASIC FLUID DYNAMICS	6
3.1. REYNOLDS TRANSPORT THEOREM	6
3.2. THE GOVERNING EQUATIONS	6
3.2.1. <i>Conservation of Mass</i>	6
3.2.2. <i>Conservation of Momentum</i>	7
3.2.3. <i>Conservation of Energy</i>	7
3.3. BERNOULLI'S EQUATION	7
3.4. INCOMPRESSIBLE AND ISOTHERMAL FLOW	7
3.5. TURBULENT FLOW	8
3.6. AERODYNAMIC FORCES	8
3.6.1. <i>Aerodynamic Drag</i>	8
3.6.2. <i>Aerodynamic Lift</i>	9
4. COMPUTATIONAL FLUID DYNAMICS – CFD	10
4.1. REYNOLDS AVERAGED NAVIER-STOKES - RANS.....	10
4.2. TURBULENCE MODELLING: REALIZABLE K-E	11
4.3. NEAR WALL-TREATMENT	12
4.4. RADIATOR MODELLING	13
4.5. FINITE VOLUME METHOD - FVM.....	14
5. METHODOLOGY	15
5.1. SOFTWARES.....	15
5.1.1. <i>CATIA V5</i>	15
5.1.2. <i>ANSA</i>	15
5.1.3. <i>STAR-CCM+</i>	15
5.2. COURSES IN STAR-CCM+	16
5.2.1. <i>Vehicle External Aerodynamics Distance Learning Course</i>	16
5.2.2. <i>Four Day STAR-CCM+ Distance Learning Course</i>	16
5.3. PRE-PROCESSING	16
5.3.1. <i>CATIA V5</i>	16
5.3.2. <i>ANSA</i>	18
5.3.3. <i>STAR-CCM+</i>	21
5.4. SOLVING	23
5.4.1. <i>Zero-Angles</i>	24
5.4.2. <i>Varying Yaw Angle</i>	25
5.4.3. <i>Varying Pitch Angle</i>	26
5.4.4. <i>Varying Roll Angle</i>	27

5.5. POST PROCESSING	27
5.5.1. Scenes.....	27
5.5.2. Reports	28
6. RESULTS	29
6.1. ZERO-ANGLES	29
6.2. VARYING YAW ANGLE.....	31
6.3. VARYING PITCH ANGLE	33
6.4. VARYING ROLL ANGLE.....	35
7. ANALYSIS OF THE RESULTS	37
7.1. ZERO-ANGLES	37
7.1.1. Drag.....	37
7.1.2. Lift.....	39
7.1.3. 120 km/h.....	40
7.2. VARYING YAW ANGLE.....	40
7.2.1. Drag.....	40
7.2.2. Lift.....	41
7.3. VARYING PITCH ANGLE	43
7.3.1. Drag.....	43
7.3.2. Lift.....	43
7.4. VARYING ROLL ANGLE.....	46
7.4.1. Drag.....	46
7.4.2. Lift.....	47
8. DISCUSSION	49
8.1. METHODOLOGY AND GENERAL WORKFLOW	49
8.1.1. Pre-Processing	49
8.1.2. Solving	49
8.1.3. Post-Processing	49
8.2. SOURCES OF ERRORS.....	50
8.2.1. Geometries.....	50
8.2.2. Computational Simplifications and Approximations.....	51
9. CONCLUSION	52
9.1. RECOMMENDATIONS FOR FUTURE WORK.....	52
10. BIBLIOGRAPHY	53
12. FIGURE REFERENCES	54
APPENDIX A	55
APPENDIX B	56

1. Introduction

The background and the aim of this project are presented in this section as well as the project's delimitations.

A Bachelor Thesis from 2013, for reference see *bibliography page 52*, was carried out to model and simulate two Silver Arrows (Auto Union Type C and Mercedes-Benz W25, *figure 1*) with the following objectives.

- *“How good is the aerodynamic performance of the cars regarding lift and drag?”*
- *What are the differences in aerodynamic performance between the cars?*
- *Are there any weak aerodynamic areas on the cars?*
- *How does the Silver Arrows' aerodynamic properties compare to their competitors' and more modern vehicles?”*



Figure 1 - The two CMC models of the Silver Arrows, which this project aims to analyse. Mercedes-Benz W25 (left), Auto Union Type C (right).

Last years thesis did not have access to CAD models and data of the two Silver Arrows; it had to be made from scratch. Using two CMC models, one for each car provided by the Department of Applied Mechanics, scaled 1:18, two models of the cars was made in CATIA V5. Due to the amount of work that was given to the models, flow simulation and analysis in STAR-CCM+ was not given the amount of time needed. The group was therefore not able to perform the simulations at different velocities and all angles were set to zero degrees in the simulations. Internal parts, such as the engines, were simplified in the CAD-models as well as certain parts in the exterior of both cars. Since the flow of air passes through the engine compartment, front grill and air intakes, these details in combination with the factors mentioned above must be taken into consideration whilst analysing the flow.

This project will focus on refining the results of the aerodynamic forces with more simulations and extensive analysis at different pitch, yaw and roll angels and at different velocities. With results from the simulations and flow analysis, the aerodynamic performance of the two Silver Arrows might be determined. Both Mercedes-Benz W25 and Auto Union Type C differed in their design, from now on mentioned as Mercedes-Benz and Auto Union. The Auto Union was a mid-engine based design with a supercharged V16 engine while Mercedes-Benz was a supercharged inline engine with eight cylinders placed in front of the driver.

Though both were semi streamlined, in order to reduce drag, their design presumably had different effect on the aerodynamic performance. From an engineer and designer's point of view it is of great interest to analyse aerodynamic performance. Using 21st century engineering tools to evaluate 1930's engineering design can help us to better understand how the Silver Arrows performed and what made them so famous both then and now. More of the history of Silver Arrows can be found in the next section, *Historical background, page 3*.

1.1. Objective

The overall aim is to conduct flow analysis of the Auto Union and the Mercedes-Benz through refined computer designed models. This will be done with a higher level of detail in the engine compartment and the undercarriage of the car. The focus will be on running more simulations in order to achieve accurate results. The project is also about analysing the aerodynamic performance at different angles of the incoming wind subjected to the car, which can be equivalent to scenarios such as acceleration, braking and cornering of a race car. The objectives are listed as follows:

- To compare and calculate lift and drag forces of two Silver Arrows with:
 - Different velocities and pitch, yaw and roll angles at zero degrees
 - Constant velocity at 80 km/h and different yaw, pitch and roll angles
 - Higher level of detail to the models
- To determine based on the CMC-models which one of the Silver Arrow race cars that is the better one in an aerodynamic perspective

1.2. Delimitations

In order to constrain the problems in this project certain delimitations have been made:

- The project is carried out from 2014-01-27 to 2014-06-02
- Thermodynamic effects will not be taken to account, e.g. heat generated from engine, when simulations is carried out
- The number of cells used in the volume mesh, in STAR-CCM+, is limited to 10-15 million
- Certain details of the cars will be modelled with simplifications
- No transient simulations of the race cars will be simulated

2. Historical Background

This section contains a brief introduction to the history of the well-known Silver Arrows. The focus of the section will be on the aerodynamics related to these cars.

As early as in the 1920's, a German aeroplane engineer-to-be, called Edmund Rumpler designed a car body for Benz. The car was called *Tropfen-Auto*, which roughly translates to drop car, see *figure 2*. The car was a major breakthrough when it comes to aerodynamics, and the teardrop shape lead to low drag. Designs like these were never before seen in racing. (Pritchard, 2008)

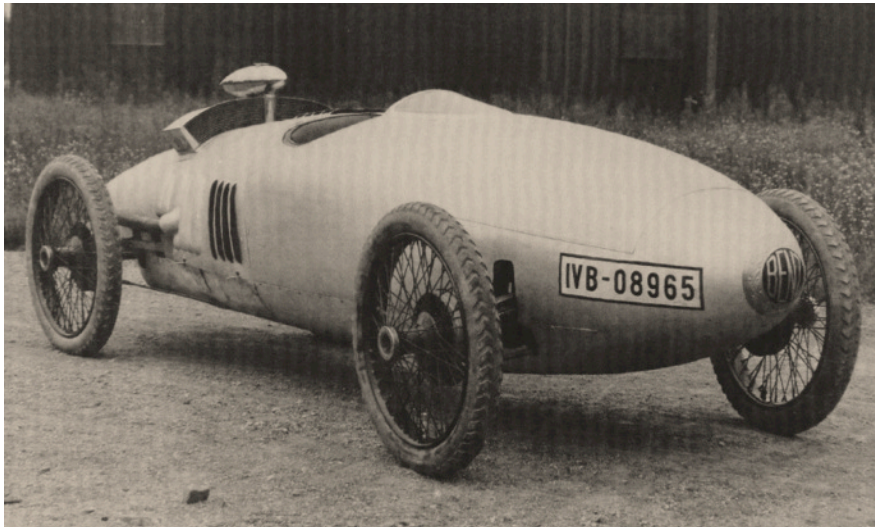


Figure 2 - The "Tropfen-Auto" also known as the "drop car" (Pritchard, 2008).

The engineers and designers, who worked on race cars in the 1930's, knowledge about aerodynamics originated mostly from aircraft design, just like Rumpler's. Great emphasis was placed on minimizing drag force, which is important in order to achieve higher velocity and acceleration. In the racing world of today there is however another force that is equally important, and that is lift, or negative lift called downforce. In the 1930's, the importance of this aerodynamic force, that affects handling and cornering speed, was generally not known. (Pritchard, 2008)

In the early 1930's engineers developed engines at a high pace, aerodynamics and handling in general was not keeping up. The cars basically had too much power and therefore were almost impossible to drive. As a reaction to this, the car companies started to experiment both with aerodynamic and chassis design. For example, Reinhard König-Fachsenfeld, a pioneer in aerodynamics, designed a car body for the 1932 *Automobil-Verkehrs- und Übungsstraße* (AVUS) race. This car had numerous improvements for decreased drag and it is fair to say that this contributed to its victory.

Some of these improvements were to be seen in later cars, but factors as changes in requirements regarding minimal cross section affected the total outcome and compliance of his design. (Pritchard, 2008)

The history of Grand Prix racing, predecessor to today's F1 racing, began at the turn of 20th century. In the early era of motor racing, the French car manufacturers dominated the races with brands such as Bugatti and Renault. Later in the 1920's the Italian manufactures such as Alfa Romeo and Maserati outrivaled the French. (Pritchard, 2008)

In the 1930's, the German car manufactures Mercedes Benz and Auto Union (today known as Audi) entered the spotlight with their unique race cars which would be remembered as the

Silver Arrows. The nickname for these cars were by the German press named “die Silberpfeile”, meaning Silver Arrows in English due to the visible aluminium bodywork, which had no paint (Figure 3, Figure 4). The reason for having no paint is according to the new regulations for the 1934 season. (Pritchard, 2008)



Figure 3 – Auto Union Type C (Pritchard, 2008).

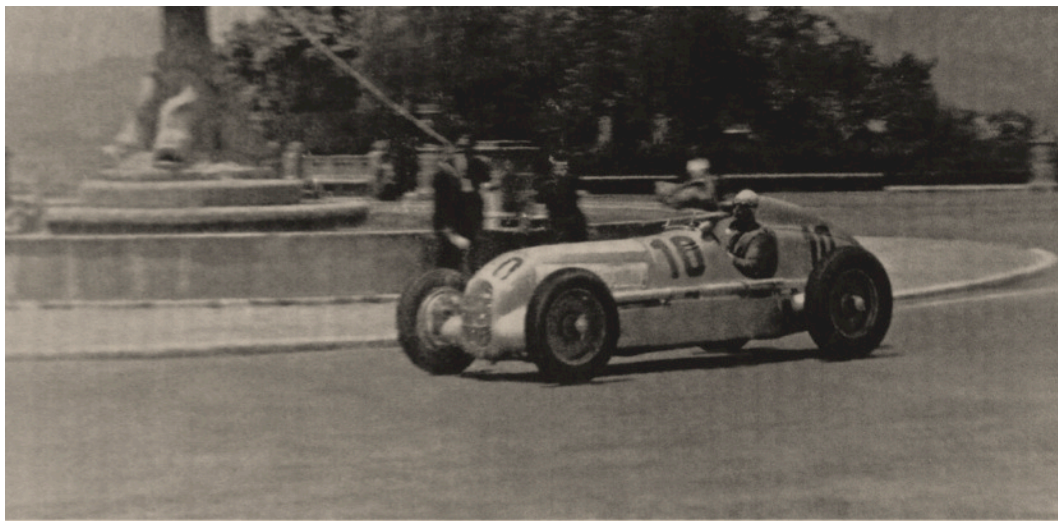


Figure 4 – Mercedes-Benz W25 (Pritchard, 2008).

When Mercedes-Benz entered with their W25 it had white colour paint, which was the official racing colour for Germany. Its dry weight, excluding tyres, fuel, oil, coolant and driver, was slightly above 750 kg, which was the limit for entering the race. The idea came up to strip the car of its body paint, and the car passed the weight limit. From then on silver became the official German racing colour. Auto Union entered with their Type C in 1936, whose design was the brainchild of Ferdinand Porsche, the man behind Volkswagen Type 1 and the company Porsche AG. The car would claim 17 victories between 1936 and 1937. (Pritchard, 2008)

In the beginning, the cars were not designed with good aerodynamic. However throughout the 1930's cars have been specially designed for special races with focus on reducing drag. This implies that the engineers developed their knowledge in the field simultaneously as the cars improved. Making small improvements and testing them in the Grand Prix series seemed like the way of doing and testing at the time. There was though one race per year where the

aerodynamicists had the opportunity to show off. This race was the AVUS race and the shape of the course forced the manufacturers to improve their cars to achieve lower drag in order to win. (Pritchard, 2008)

As mentioned before, the trend started in 1932 by König-Fachsenfeld got more and more extreme each year. In the AVUS race 1934, both the Alfa Romeo team and the Ferrari team entered with modified cars that were designed by the Italian fighter aircraft designer *Ing.* Cesare Pallavicino. The streamlined Alfa Romero, *figure 5*, with Guy Moll behind the wheel won. Worth to mention is the lack of aerodynamic improvements at Auto Union, they participated with one of their usual racing cars (type A). (Pritchard, 2008)

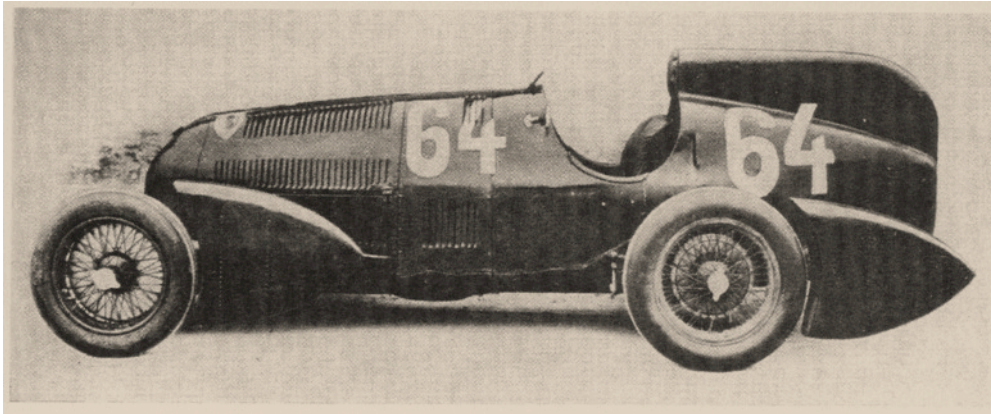


Figure 5 - The Alfa Romeo designed by Pallavicino used in the AVUS race (Pritchard, 2008).

The year after, 1935, Auto Union entered with both usual racing cars and a streamlined edition. Unfortunately, the engine of that car failed and no conclusion of aerodynamic influence in general can be drawn. Mercedes-Benz entered with non-modified cars and won. In 1936, something best described as a paradigm shift took place. Both Auto Union and Mercedes-Benz entered with several streamlined cars as well as more standard looking race cars. The new cars had covered wheels, long sweeping bodies and small grilles. (Pritchard, 2008)

From 1934 to 1939, the Grand Prix races would be a race primarily between Auto Union and Mercedes-Benz as they out qualified their other competitors in terms of speed and acceleration. The cars would be developed throughout the 1930's and would continue to dominate the Grand Prix races and they would also set land speed records. The Second World War would halt their dominance in motor racing. However in 1950, the Germans would be readmitted to motor racing. Auto Union, did not enter the races, but Mercedes-Benz did. They would score some victories with new models, but their participation would come to an abrupt halt. In 1955, at Le Mans 24 hour race, Mercedes-Benz was involved in a tragic accident which caused their car to hurtle into the spectators, killing 83 people and injuring more than 100. The disaster contributed to Mercedes-Benz withdrawal from motor racing. It would not be until 2010 that Mercedes-Benz returned to F1 racing. (David, 1999)

3. Basic Fluid Dynamics

This section presents the basic fluid dynamics theory used in this project to calculate aerodynamic forces with computational fluid dynamics (CFD). All theory presented is necessary and used in this project.

Both liquids and gases are classified as fluids and fluid dynamics is the study of these in motion. Fluid dynamics itself has a wide range of applications and practically everything on this planet is either a fluid or moves around a fluid. This makes the calculations regarding fluid dynamics important.

Fluid dynamics is a sub discipline of fluid mechanics and therefore satisfies a great set of well-known basic laws, and thus a great deal of theoretical treatment is available for calculations. However the theory is often incorrect due to the fact that it applies mainly to idealized situations, which partly is invalid in reality. The most common used basic laws utilized to calculate fluid dynamics is presented below. (Bulut, 2006)

3.1. Reynolds Transport Theorem

Reynolds Transport Theorem is one of the most important formulas for calculating fluid dynamics thus it can be applied to all the basic laws. It can be simply stated as, the original volume of the control volume and what enters and leaves. Basically it is a control volume where you calculate on the existing volume and the in- and outlets. The general formula for Reynolds transport theorem is:

$$\frac{d}{dt}(B_{sys}) = \frac{d}{dt}(\int_{CV} \beta \rho dV) + \int_{CS} \beta \rho V \cos \theta dA_{out} - \int_{CS} \beta \rho V \cos \theta dA_{in} \quad (\text{Eq. 1})$$

Where $\frac{d}{dt}(B_{sys})$ is the time rate of change of B within the system, $\frac{d}{dt}(\int_{CV} \beta \rho dV)$ is the time rate of change of B within the control volume and $\int_{CS} \beta \rho V \cos \theta dA_{out} - \int_{CS} \beta \rho V \cos \theta dA_{in}$ is the in- and outflow to the control surface. (White, 2011)

3.2. The Governing Equations

Reynolds transport theorem establishes a relation between system rates of change and control volume surface and volume integrals. Changing the variable B into, respectively, mass, momentum and energy gives three new formulas called the conservation laws, also called the governing equations of fluid dynamics, as presented below. Together they can describe any flow and are the cornerstone of computational fluid dynamics.

3.2.1. Conservation of Mass

Replacing B to m and β to $dm/dm = 1$ gives a new formula called the conservation of mass:

$$\frac{dm}{dt}_{sys} = 0 = \frac{d}{dt}(\int_{CV} \rho dV) + \int_{CS} \rho(\mathbf{V}_r \cdot \mathbf{n})dA \quad (\text{Eq. 2})$$

The law states that for any system closed to all transfers of matter and energy, the mass of the system must remain constant over time. That is because the system mass cannot change quantity if it is not added or removed. This implies that mass can neither be created nor destroyed. (White, 2011)

3.2.2. Conservation of Momentum

In a closed system, the total momentum is constant. Imagine two particles interacting, from Newton's third law of motion the forces between them must be equal, and the force is according to the second law stated as the force is equal to the linear momentum change over time, $F = \frac{dp_l}{dt}$. Therefore with equal force we have $\frac{p_{l1}}{dt} = \frac{p_{l2}}{dt}$. Simply explained, if two objects are occurring in the same isolated system, the total momentum after the collision is equal to the total momentum before the collision. By changing B to $m\mathbf{V}$ and β to $dB/dm = \mathbf{V}$ in equation 1 the formula is: (White, 2011)

$$\frac{d}{dt}(m\mathbf{V}_{sys}) = \Sigma F = \frac{d}{dt}(\int_{CV} \mathbf{V}\rho dV) + \int_{CS} \mathbf{V}\rho(\mathbf{V}_r \cdot \mathbf{n})dA \quad (\text{Eq. 3})$$

3.2.3. Conservation of Energy

The law of conservation of energy states that "Energy cannot be created nor destroyed, it can only be changed from one form to another". In fluid dynamics this means that the total energy of an isolated system cannot change, thus it is conserved over time. From Reynolds transport theorem and with the change B to E and β to $dE/dm = e$ the formula is: (White, 2011)

$$\left(\frac{dE}{dt}_{sys}\right) = \frac{d}{dt}(\int_{CV} e\rho dV) + \int_{CS} e\rho(\mathbf{V} \cdot \mathbf{n})dA \quad (\text{Eq. 4})$$

3.3. Bernoulli's Equation

The Bernoulli equation relates pressure, velocity and potential energy into one equation:

$$P_1 + \frac{\rho V_1^2}{2} + \rho g z_1 = P_2 + \frac{\rho V_2^2}{2} + \rho g z_2 = constant \quad (\text{Eq. 5})$$

The Bernoulli equation is derived from force equilibrium on a particle moving along a streamline with a few restrictions such as; steady flow, incompressible flow and frictionless flow. In many Bernoulli analyses, the elevation change is negligible which reduces the Bernoulli equation to an equation regarding just velocity and pressure: (White, 2011)

$$P_1 + \frac{\rho V_1^2}{2} = P_2 + \frac{\rho V_2^2}{2} = P_0 = constant \quad (\text{Eq. 6})$$

From this reduced Bernoulli equation and with the above restrictions in mind, it is easy to see that lower pressures relates to higher velocities and vice versa. (White, 2011)

3.4. Incompressible and Isothermal Flow

All fluids are in some matter compressible, this means that the density will change after changes in pressure or/and temperature. Calculating on compressible flows is far more complex than incompressible flow and in many situations the changes in pressure and temperature are relatively small so the changes in density can be negligible. An explicit criterion for incompressible flow is:

$$\frac{V}{a} = Ma \leq 0.3 \quad (\text{Eq. 7})$$

For air at standard conditions, a flow can thus be considered incompressible if the velocity is less than 100 m/s, equal to 360 km/h. Hence, in this project it is assumed that the air is incompressible, meaning that the air density will remain constant throughout the whole simulation.

The temperature is also assumed to be constant over the vehicle due to the large volume of air surrounding the vehicle. This is a normal assumption and a constant temperature gradient gives a constant viscosity, which simplifies the calculations. Because of this the flow is considered isothermal. (White, 2011)

3.5. Turbulent Flow

A flow can appear either laminar or turbulent. A laminar flow occurs when a fluid flows in parallel boundary layers without any disturbance and eventually dies out due to loss of kinetic energy. This is not the case for a race car and the simulation in this project will therefore assume turbulent boundary layer flow, due to the high speed. A turbulent flow is characterized by chaotic rapid variations of pressure and velocity over time and Reynolds number over 10^6 for open flow. Reynolds number is determined by:(White, 2011)

$$Re = \frac{\rho VL}{\mu} = \frac{VL}{\nu} \quad (\text{Eq. 8})$$

3.6. Aerodynamic Forces

Fluid dynamics has several sub disciplines such as aerodynamics, which is the study of air in motion, particularly when it interacts with a solid object, in this case a race car. With its movement, a vehicle displaces the surrounding air. That pressure field generated by the airflow is the dominant reason for the aerodynamic forces experienced by the vehicle. The aerodynamic forces of interest in this bachelor thesis are lift and drag. Side forces are also an important factor affecting the stability of the vehicle, but they are hard to predict and model. Lift and drag are forces due to air flow surrounding the vehicle. The resultant of these three force vectors gives the total aerodynamic force. These aerodynamic forces vary a lot depending on the type of vehicle, but most commonly modern sport cars are designed to have a negative lift force, called downforce, and a minimized drag force. (Katz, 1995)

3.6.1. Aerodynamic Drag

Having a minimized drag force is as earlier mentioned something to aim for. One reason is its positive effects on lowering the fuel consumption, another is to increase the acceleration and top speed.

Drag forces are a type of resistance, working in opposite direction to the motion of the car. As mentioned, the drag depends on pressure difference, but it also depends on skin friction. Most of the drag is generated by a car is due to pressure difference between the front and the rear. To minimize pressure drag, it is important to have as much attached flow as possible over the car. A typical good design in drag aspect is boat tailing, which makes the rear pointy and make sure that the air is attached. The friction between a car and the air is quite small, but it is hard to get rid of. A consequence of having attached flow over the body is that the skin friction can be increased, but the increase of friction is much less than the decrease of pressure difference. Overall it can be said that a smoother surface leads to a smaller skin friction.

The drag force depends on the fluids properties and the shape of the object. C_D is a dimensionless parameter that describes how much drag a body is generating according to the following equation:

$$C_D = \frac{2F_{Drag}}{\rho v^2 A_P} \quad (\text{Eq. 9})$$

This parameter is of great importance and should always be optimized. Changing the geometry of the car could for example do it. C_D is a consequence of pressure difference and friction as the following equations show. (White, 2011; Katz, 1995)

$$C_D = C_p + C_f \quad (\text{Eq. 10})$$

$$C_p = \frac{p - p_\infty}{\frac{1}{2}\rho V_\infty^2} \quad (\text{Eq. 11})$$

$$C_f = \frac{\tau_{wall}}{\frac{1}{2}\rho V_\infty^2} \quad (\text{Eq. 12})$$

3.6.2. Aerodynamic Lift

Lift force is the force working against gravity, i.e. when a race car drives forward, the lift force will try and lift the car upwards. Modern race cars aim to have a high negative lift force, called downforce, to achieve sufficient grip.

Lift occurs when the air speed is higher on top of the car than under. This gives a lower pressure on top of the car that lifts the car up. Since downforce is the desired force a lower pressure is wanted underneath the car also called a ground effect. Downforce can for example be generated by having low ground proximity to increase the speed underneath, or by adding wings to control the airflow. A rear wing added will increase the coefficient of drag due to a larger area of exposure towards the wind, but this is a penalty worth paying in motorsport (White, 2011; Katz, 1995).

C_L is a dimensionless factor describing how much lift a particular body is generating, and is given by:

$$C_L = \frac{F_{Lift}}{\frac{1}{2}\rho V_\infty^2 A} \quad (\text{Eq.13})$$

It is generally more important to know where the lift is high or low, therefore C_L is usually split onto the two axles with the corresponding coefficients, $C_{L \text{ front}}$ and $C_{L \text{ rear}}$ to get a better understanding of the lift ratio.

4. Computational Fluid Dynamics – CFD

Computational Fluid Dynamics is a widely used method to calculate aerodynamic problems. In this section, the theory used in this project regarding CFD is presented.

The main obstacles that occur while calculating fluid dynamics are problems regarding the geometry and viscosity. The basic equations are far too complicated to let one analyse the arbitrary geometric configurations. The viscosity has a destabilizing effect on fluids, giving rise of pressure even at very low velocities with a consequence of disorderly random phenomenon also called turbulence. It is virtually impossible to calculate complex geometry analytically. The traditional tools used in the industry to evaluate aerodynamics performance of cars are wind tunnel and road tests. These test are very expensive and sometimes have limitations in reality, therefore numerical programs such as CFD are necessary. (Wilcox, 1994)

4.1. Reynolds Averaged Navier-Stokes - RANS

The Navier-Stokes equations are special cases of the conservation laws and describe a fluid in motion. The incompressible Navier-Stokes equations are commonly used to model incompressible turbulent flow. The majority of flows whom has no analytical solution may obtain a solution through the use of numerical method such as CFD-computational fluid dynamics that is used in this thesis.

CFD simulation can entail enormous computational effort due to the fact that the smallest eddies in a turbulent flow shrink in size as the Reynolds number increase, thereby requiring very small grid spacing in the discretization. The vast majority of solutions to the turbulent flow are therefore not obtained by solving the actual Navier-stokes equations. Instead the program used in this thesis uses a modified version of Navier-Stokes in which the unsteady terms are dropped and the effect of turbulence is modelled. These modified equations are called the Reynolds Averaged Navier-Stokes equations. (Wilcox, 1994; White, 2011)

The Reynolds Averaged Navier-Stokes equations describe fluid flow in motion, but the simplifications of the equations only give the time-averaged motion (White, 2011). The idea behind is Reynolds decomposition, which is a technique to separate the average and the fluctuating parts of a quantity, *figure 6*.

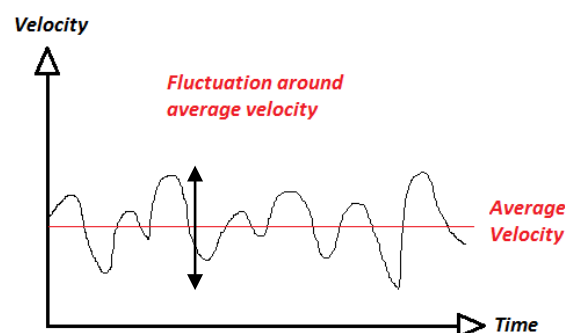


Figure 6 – Averaged Navier-Stokes with both average and fluctuation terms.

The bar over the values indicates the averaged part and the prime the fluctuating part (Eq. 14-17). The mean value over time is integrated over a long period such that the averaged part is time invariant and the time average of the fluctuating part is equal to zero. The true time average of a velocity vector $\mathbf{V}=(u,v,w)$ can be seen below:

$$u = \bar{u} + \acute{u} \quad (\text{Eq.14})$$

$$v = \bar{v} + \acute{v} \quad (\text{Eq.15})$$

$$w = \bar{w} + \acute{w} \quad (\text{Eq.16})$$

$$p = \bar{p} + \acute{p} \quad (\text{Eq.17})$$

$$\bar{u} = \lim_{T \rightarrow \infty} \frac{1}{T} \int_{t_0}^{t_0+T} u dt \quad (\text{Eq.18})$$

The continuity equation for incompressible flow then gives:

$$\frac{\partial u}{\partial x} + \frac{\partial v}{\partial x} + \frac{\partial w}{\partial x} = \frac{\partial(\bar{u}+\acute{u})}{\partial x} + \frac{\partial(\bar{v}+\acute{v})}{\partial x} + \frac{\partial(\bar{w}+\acute{w})}{\partial x} = 0 \quad (\text{Eq.19})$$

Average equation 19 gives:

$$\frac{\partial(\bar{u}+\acute{u})}{\partial x} + \frac{\partial(\bar{v}+\acute{v})}{\partial x} + \frac{\partial(\bar{w}+\acute{w})}{\partial x} = \frac{\partial \bar{u}}{\partial x} + \frac{\partial \bar{v}}{\partial x} + \frac{\partial \bar{w}}{\partial x} = 0 \quad (\text{Eq.20})$$

The Reynolds Averaged Navier Stokes in x-direction is then written as:

$$\rho \left(\frac{\partial \bar{u}}{\partial t} + \bar{u} \frac{\partial \bar{u}}{\partial x} + \bar{u} \frac{\partial \bar{v}}{\partial y} + \bar{u} \frac{\partial \bar{w}}{\partial z} \right) = \frac{\partial p}{\partial x} + \mu \left(\frac{\partial^2 \bar{u}}{\partial x^2} + \frac{\partial^2 \bar{u}}{\partial y^2} + \frac{\partial^2 \bar{u}}{\partial z^2} \right) - \rho \left(\frac{\partial \overline{uu}}{\partial x} - \frac{\partial \overline{uv}}{\partial y} - \frac{\partial \overline{uw}}{\partial z} \right) \quad (\text{Eq.21})$$

Reynolds stresses

The Reynolds stresses then can be written as:

$$\rho \left(\frac{\partial \overline{uu}}{\partial x} - \frac{\partial \overline{uv}}{\partial y} - \frac{\partial \overline{uw}}{\partial z} \right) = \frac{\partial}{\partial x_j} (\rho u_i u_j) \quad (\text{Eq.22})$$

Where $\overline{u_i u_j}$ represent the Reynolds stresses. These equations, the Reynolds Averaged Navier Stokes in x, y and z-direction and the continuity equation, is a problem of four equations and ten unknown variables. To solve this problem we need to model the Reynolds stresses. (Pope, 2000; White, 2011)

4.2. Turbulence Modelling: Realizable $k - \epsilon$

The use of turbulence modelling is necessary for calculating complex problems of fluid dynamics. The idea is to construct a model to predict the turbulence behaviour of a fluid. There are a wide range of different models for this purpose; in this project a model called realizable $k - \epsilon$ is used which is based on the Reynolds Averaged Navier-Stokes equations with the Boussinesq assumption (Eq. 23). This assumption proposes that the Reynolds stresses earlier mentioned can be modelled by the mean rate of deformation, this by introducing a new property called eddy viscosity, μ_t . (Dr. Subhendu Maity, 2011; Pope, 2000)

$$\tau_{ij} = \overline{(\rho u_i u_j)} = 2\mu_t S_{ij} - \frac{2}{3}\rho k \delta_{ij}, \quad S_{ij} = \frac{1}{2} \left(\frac{\partial u_i}{\partial x_j} + \frac{\partial u_j}{\partial x_i} \right) \quad (\text{Eq.23})$$

The use of this assumption is a huge simplification, but it allows one to think of the effect turbulence flow have on the overall flow. This can be compared with the molecular viscosity effects on a laminar flow.

In the two-equation model $k - \varepsilon$, the previously mentioned eddy viscosity depends on a structure parameter C_μ , the turbulent kinetic energy, k and the turbulent kinetic energy dissipation rate ε .

$$\mu_t = \rho C_\mu \frac{k^2}{\varepsilon} \quad (\text{Eq.24})$$

All information of the Reynolds stresses is now contained in this non dimensional rather complex structure parameter C_μ . It is therefore of high importance to model this parameter accurately. There are two different ways to model this parameter, the standard model and the realizable $k - \varepsilon$ model. The only difference between a standard and a realizable $k - \varepsilon$ is the way this structure parameter is calculated. In the standard model the structure parameter is set to $C_\mu = 0,09$ but in the realizable model the structure parameter is calculated as follows:

$$C_\mu = \frac{1}{A_0 + A_S \frac{kU^*}{\varepsilon}} \quad (\text{Eq.25})$$

The transport Equations can be written with earlier mentioned assumptions as:

$$\frac{\partial}{\partial t}(\rho k) + \frac{\partial}{\partial x_j}(\rho k u_j) + \frac{\partial}{\partial x_j} \left[\left(\mu + \frac{\mu_t}{\sigma_k} \right) \frac{\partial k}{\partial x_j} \right] + P_k + P_b - \rho \varepsilon - Y_M + S_k \quad (\text{Eq.26})$$

$$\frac{\partial}{\partial t}(\rho \varepsilon) + \frac{\partial}{\partial x_j}(\rho \varepsilon u_j) + \frac{\partial}{\partial x_j} \left[\left(\mu + \frac{\mu_t}{\sigma_\varepsilon} \right) \frac{\partial \varepsilon}{\partial x_j} \right] + \rho C_1 S \varepsilon - \rho C_2 \frac{\varepsilon^2}{k + \sqrt{v \varepsilon}} + C_{1\varepsilon} \frac{\varepsilon}{k} C_{3\varepsilon} P_b + S_\varepsilon \quad (\text{Eq.27})$$

4.3. Near Wall-Treatment

The viscous sublayers are not resolved with the $k - \varepsilon$ method due to steep pressure and velocity gradients in the region. Also the layers are dominated by laminar shear and turbulence models are not applicable where the viscous effects dominate. To get an accurate result the mesh cells would have to be very small and it would increase the computation time severely. Instead of increasing the amount of cells, near wall-treatment is used.

A logarithmic relation has been established that states that the average velocity of a turbulent flow at a certain point is proportional to the logarithm of the distance from that point to the wall or the boundary of the fluid (White, 2011). The log-law region correspond to the logarithmic relation:

$$u^+ = \frac{1}{\kappa} \ln(y^+) + C^+ = \frac{u}{u_\tau} \quad (\text{Eq.28})$$

$$y^+ = \frac{y \sqrt{\tau_w}}{\nu \sqrt{\rho}} \quad (\text{Eq.29})$$

With dimensions, the logarithmic law of the wall can be written as:

$$u = \frac{u_\tau}{\kappa} \ln \frac{y}{y_0} \quad (\text{Eq.30})$$

The log-law is valid for $30 < y^+ < 400$. The near wall region is divided into two additional zones called the viscous sublayer and the buffer layer. They correspond to $5 < y^+ < 30$ for the buffer layer and $y^+ < 5$ for the viscous sublayer. In the viscous sublayer, the variation between u^+ and y^+ is approximately 1,1 and it is therefore assumed that $y^+ = u^+$. In the buffer layer neither law holds.

There is a wide range of different wall functions to use to calculate the flow in the viscous sublayer. Two of these, the standard wall function and the non-equilibrium wall function, are commonly used in commercial CFD softwares. The standard wall function calculates the velocity near the wall as: (Kim, et al., 1995)

$$u^+ = \frac{1}{\kappa} (E_k y^+) \quad (\text{Eq.31})$$

$$u^+ \equiv \frac{U_p C_\mu^{1/4} k_p^{1/2}}{\tau_w / \rho} \quad (\text{Eq.32})$$

$$y^+ = \frac{\rho C_\mu^{1/4} k_p^{1/2} y_p}{\mu} \quad (\text{Eq.33})$$

The non-equilibrium wall function is a two-layer wall function that includes some effects of pressure gradients and strong non-equilibrium. The result is a new equation for calculating the mean velocity:

$$\frac{\bar{u} C_\mu^{1/4} k^{1/2}}{\tau_w / \rho} = \frac{1}{\kappa} \ln \left(E_k \frac{\rho C_\mu^{1/4} k^{1/2} y}{\mu} \right) \quad (\text{Eq.34})$$

Which is the mean velocity sensitized to pressure gradients and where:

$$\bar{u} = u - \frac{1}{2} \frac{\partial p}{\partial x} \left[\frac{y_v}{\kappa \rho \sqrt{\kappa}} \ln \left(\frac{y}{y_v} \right) + \frac{y - y_v}{\kappa \rho \sqrt{\kappa}} + y_v^2 \right] \quad (\text{Eq.35})$$

And y_v is the physical viscous sublayer thickness:

$$y_v = \frac{\mu y_v}{\rho C_\mu^{1/4} k^{1/2}} \quad (\text{Eq.36})$$

The non-equilibrium wall function is normally used in complex flows involving separation, reattachment and stagnation zones with rapid changes and steep pressure gradients.

4.4. Radiator Modelling

The general design of the radiator makes the flow lose pressure. To capture this complex structure of the radiator parts in CFD, a fine mesh with many cells is necessary, resulting longer simulation times. Instead of simulating a real radiator, the pressure drop can be modelled with the following equation derived from a second order polynomial. In STAR-CCM+ the inertial and viscous resistance terms are represented by ρC respectively $\frac{\mu}{\alpha}$ (Jerhamre, 2001)

$$\frac{dP}{dx} = \frac{1}{2} \rho C V^2 + \frac{1}{\alpha} \mu V \quad (\text{Eq.37})$$

4.5. Finite Volume Method - FVM

So far the earlier mentioned transportation equations cannot be solved analytically for such a complex geometry as a whole vehicle. Therefore Computational Fluid Dynamics, is used to obtain an accurate result, in this project a program named STAR-CCM+ was used (see methodology for more information). The finite volume method is one of the most adaptable discretization techniques used in CFD to solve fluid dynamics problems. The method is to separate the whole computational domain, V_{CFD} , into a number of small control volume elements, $V_{CFD} = \sum_{n \rightarrow N} V_n$. These control volume elements are usually represented as polyhedral (tetrahedron, hexahedron, prism, etc.) cells and the variable of interest is located at the centroid of the control volume.

The next step is to integrate the differential form in the earlier mentioned governing and transportation equations over each control volume element. By assuming interpolation profiles the variation of the concerned variables between the elements centroids can be solved for each element and for the total domain. This iterative procedure continues until the solutions residuals converge, less than 10^{-4} . The resulting equation received is then called the discretization equation and it expresses the conservation principle for the variable inside the control volume element. (Eymard, Gallouet, Herbin, 2003)

5. Methodology

In the following section the methodology is presented in a chronological order. First the different softwares and courses used in this project will be presented briefly, followed by the CFD workflow.

CFD processes are usually divided into three different phases, *figure 7*. The first phase is called *pre-processing* and consists of the work carried out before the simulation starts. The second is *solving* which involves the actual simulation and doing the necessary calculations. The final phase is *post-processing*, which consist of visualizing the results from the CFD simulation and analysing it.

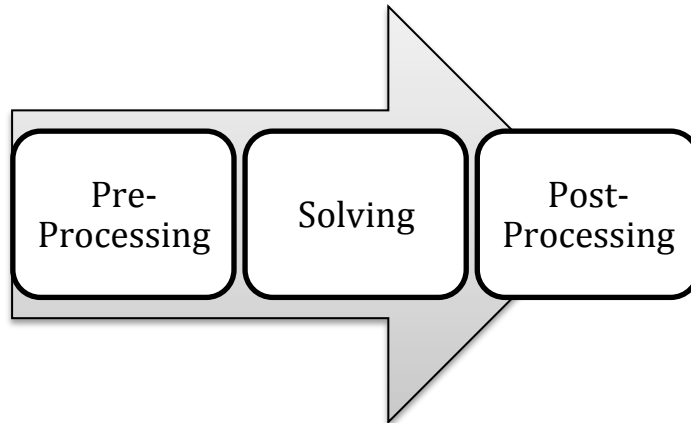


Figure 7 - Figure displaying the different phases in CFD.

5.1. Softwares

The softwares used in this thesis will be presented below.

5.1.1. CATIA V5

CATIA V5 is a common CAD program by Dassault Systems used to help engineers create virtual models. In this thesis CATIA V5 is used to construct detailed engine models for both cars, which are then exported in to ANSA. CATIA V5 is used, since this is the software used by last year's group and also because the members of this year's project are most familiar with it as well.

5.1.2. ANSA

ANSA is a pre-processing computer software by BETA CAE Systems S.A. The first reason to use this software is to adapt the CAD models for the upcoming simulations. Usually the CAD-geometry needs to be repaired; typical repair operations are closing of unwanted holes and removing intersecting surfaces. The second reason is to create a standard surface mesh (.stl) on the CAD geometry that can be imported and read by STAR-CCM+ later on. ANSA is primarily used because of the good pre-processing abilities and also because the supervisor of the bachelor project is very familiar with this software.

5.1.3. STAR-CCM+

STAR-CCM+ is a simulation software by CD-Adapco mostly known for its CFD capabilities. The standard surface mesh is imported from ANSA into STAR-CCM+ where a new surface mesh and volume mesh is created, this will be described later on. When the appropriate meshes are created, the solving is then set up and run. STAR-CCM+ also has good post-processing capabilities, hence this software will be used for all the post-processing.

5.2. Courses in STAR-CCM+

All of the group members had limited knowledge in CFD simulation at the start of the bachelor thesis, therefore two different courses given by CD-Adapco were taken to help increase the knowledge of overall CFD simulations in STAR-CCM+.

5.2.1. Vehicle External Aerodynamics Distance Learning Course

This is a more advanced course in CFD with focus on external aerodynamics for race cars with a more applied approach for all the steps in the CFD simulation.

5.2.2. Four Day STAR-CCM+ Distance Learning Course

Basic knowledge was gained in a distance course explaining the fundamentals of STAR-CCM+ through web seminars. Focusing on the three main categories in CFD, pre-processing, solving and post-processing. Under these categories the most important features were explained and how to use them appropriately.

5.3. Pre-processing

In the Pre-processing stage, the main objective is to construct CAD models of each car, which can then be used to generate the appropriate meshes. A good quality surface and volume mesh is the desired achievement in this phase.

5.3.1. CATIA V5

Part of the pre-processing involved refining the previous year made CAD models of the cars. Last year's CAD models did not give a good representation of the engine compartment of the cars. The airflow through the engine compartment affects the overall flow. Therefore, a good detailed representation of the engines was needed to improve the simulations. Improvements were also done on the bodywork of both cars. The measurements for the different parts of the engines were taken manually using callipers and eyesight from the CMC models of the cars, supplied by the Department of Applied Mechanics. Measurements were taken of both the engine parts and the gap between the parts and the bodywork to make sure that good representations of the models were made.

The engine compartment was improved by changing the engine geometry from a volume closed by a plane to one with a shape much more similar to the model, and thereby the real engine, *figure 8, page 17.*

The following parts were included in the CAD of the Auto Union engine compartment:

- Cylinder block
- Cylinder head
- Exhaust pipes and manifold
- Air intake manifold
- Compressor and carburettor
- Cooling pipes
- Fuel tank
- Part of drive shaft housing

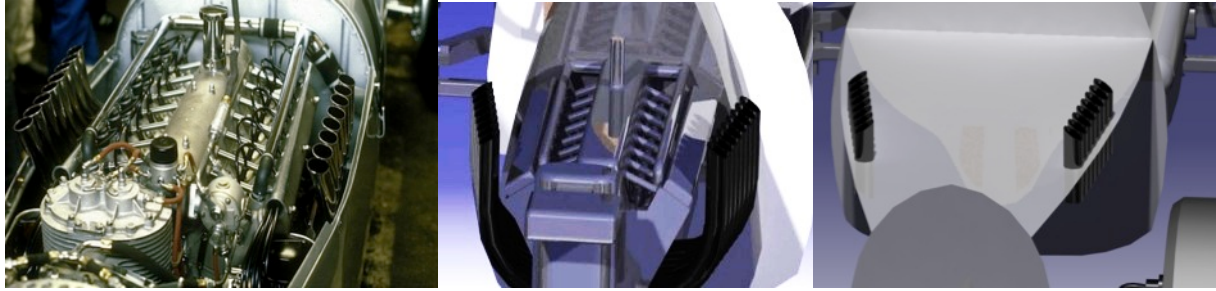


Figure 8 - The V16 engine of the Auto Union, replica (left)(Spurze, 2007), this years CAD model (middle) and previous years CAD model (right).

An air vent on the underside of the Auto Union was created by removing three faces, the change can be seen in *figure 9*.

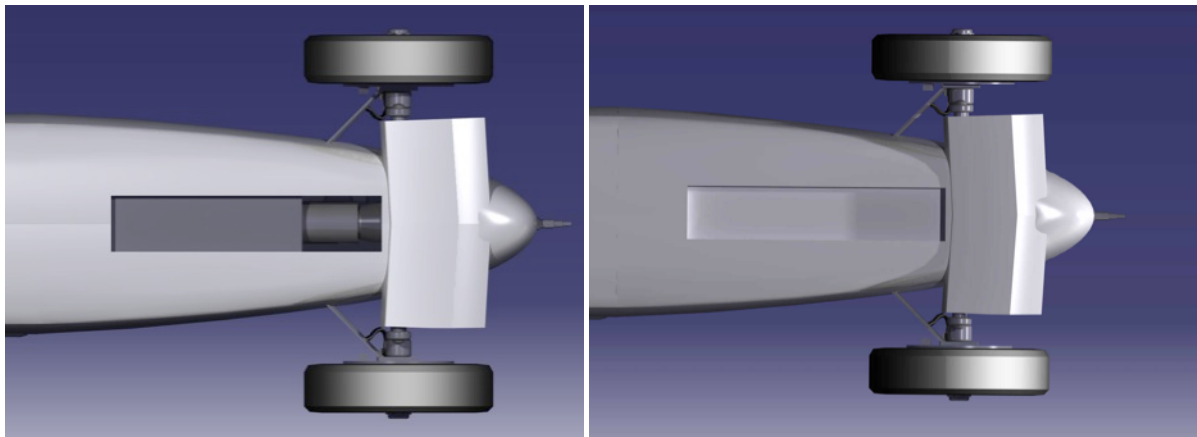


Figure 9 - Air vent on the undercarriage, new (left) and old (right).

The engine compartment in the Mercedes-Benz was earlier a simple block which gave a bad representation of the real geometry. The engine and surrounding parts were remade and resulted in an engine compartment with good similarity to the model and the real engine, *figure 10, page 18*.

The following parts were included in the CAD of the Mercedes-Benz engine compartment;

- Cylinder block
- Cylinder head
- Exhaust pipes and manifold
- Air intake manifold
- Compressor and carburettor
- Cooling pipes
- Fuel tank

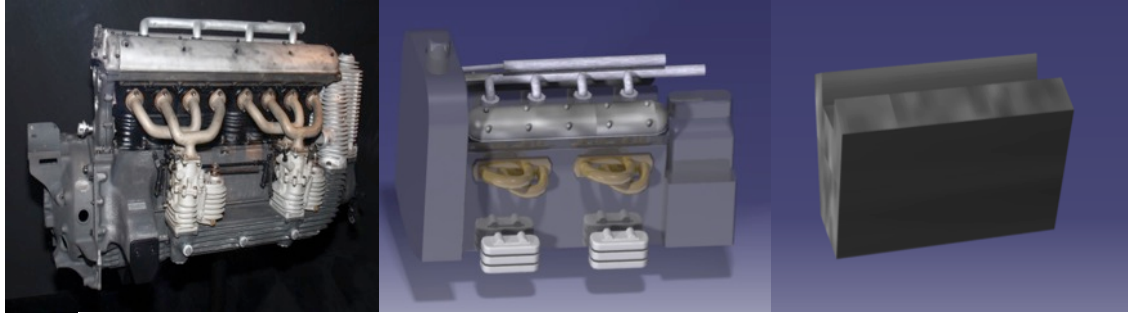


Figure 10 - The Mercedes-Benz engine, authentic (left) (Morio, 2013), this years CAD model (middle) and previous years CAD model (right).

Parts of the suspension underneath the rear axle of the Mercedes-Benz were also added as seen in *figure 11*. To see the complete CAD models for both the Auto Union and the Mercedes-Benz see appendix B.

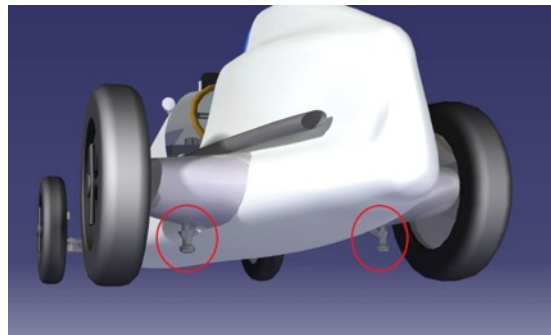


Figure 11 - Parts of the newly made suspension.

5.3.2. ANSA

The CAD models were imported into ANSA, where the geometry clean up began. Certain detail changes were made on both cars, which was difficult to add in CATIA V5. The cars were also scaled up from the model size of 1:18, to real size in ANSA. For the Auto Union a hole was added beneath the radiator, *figure 12*. A surface plane sealing off the engine room situated beneath the hood of the engine room was removed. There was also a vertical plane behind the engine, which was removed. These planes were originally there to isolate the engine compartment and thereby reduce the computer power in the processing face. This was a quite large simplification made by the previous year group, and has now been changed.

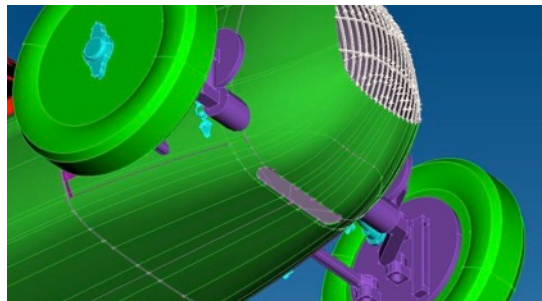


Figure 12 - The grey area between the tyres is the new hole.

At the rear of the car there are two air intakes to the engine compartment that were sealed, *figure 13, page 19*. These air intakes were sealed due to the uncertainty of the geometry below, they could lead into the engine, and since no engine flow is simulated closing them would be more realistic. If the air intakes lead somewhere else, the difference in drag would not be substantial.

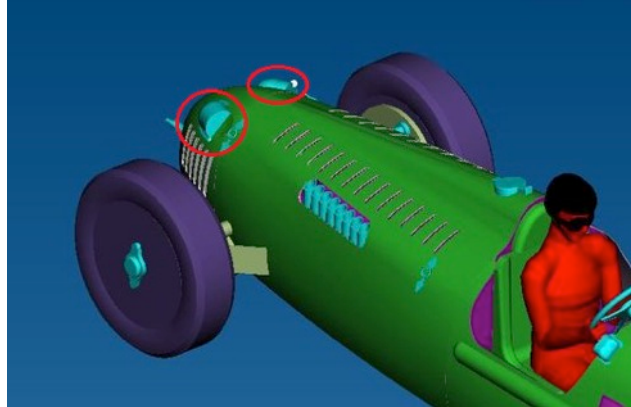


Figure 13 - The sealed air intakes can be seen inside the red circles.

A driver, used by the 2013 year group, was added in ANSA and placed in the cockpit. There were no strict constraints of the location of the driver, so the positioning was not precise. The positioning of the driver was based on pictures from previous year's report. It is important to know that the driver's position differs between this project and the project from the previous year. This difference could affect the C_D , C_L and the projected frontal area of the car. This means that some of the difference in C_D , C_L etc. compared with last year's result will be caused just by the driver.

The same problem with the driver occurred for the Mercedes-Benz as well. On the Mercedes-Benz, grill shaped holes located in the front segment of the car beneath the engine were added, previously none existing in the CAD-model. A big hole directly under the engine was also added, *see figure 14* for all new holes on the Mercedes-Benz. A wall between the radiator and the inside of the body was added to force the air through the radiator. Before this modification was made it was possible for the air to go around the radiator before entering the engine compartment.

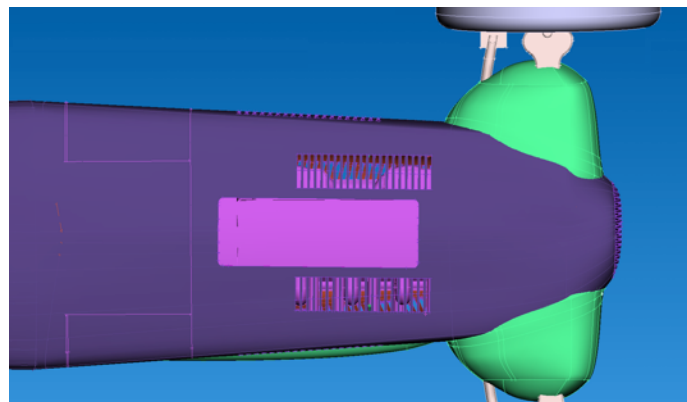


Figure 14 - All holes added to the Mercedes-Benz.

There were a lot of bad geometries discovered in ANSA that needed to be fixed. Most of the problems were surfaces that did not intersect properly and small holes in random locations. Some minor bad geometries still exist, but all crucial problems were taken care of.

Different parts of both cars needed to be grouped and assigned with a unique identity called *PID's* in ANSA, *figure 15, page 20*. The parts were assigned with *PID's* according to how coarse the mesh cell sizes would be set in STAR-CCM+. How coarse the cells would be were divided in a five grade scale were 1 is finest and 5 the most coarse cell size. Setting *PID's* is also useful for analysing mass flow, pressure and velocity on those parts separately. If the number of *PID's* are the same, have the same name and are set in the same order it is possible to import both cars into the same simulation and run that simulation for each car, it means that the settings does not need to be set for each simulation. It will save a large amount of time in the end.

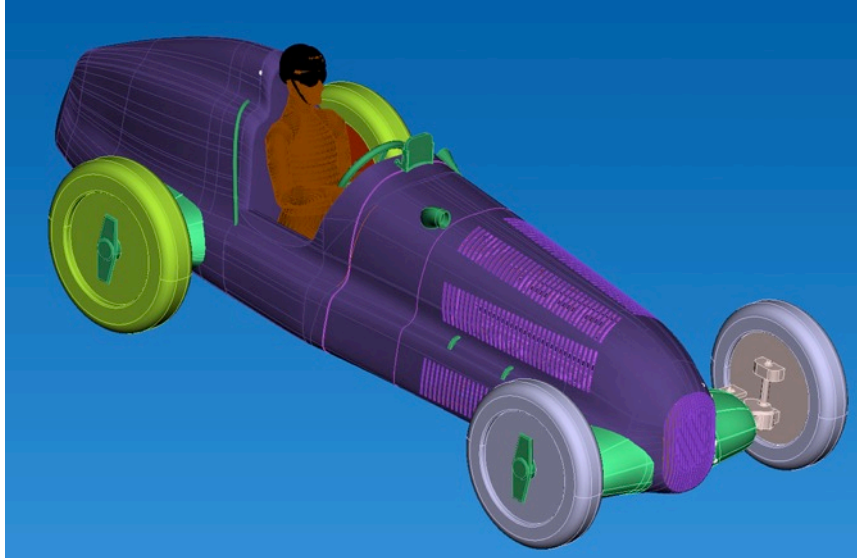


Figure 15 - The different PID's are represented by colours. See *table 1* to see what part corresponds to which colour.

The PID table below, *table 1*, shows the names that were used on the different PID's. The number at the end of each name indicates the mesh cell sizes used. The colours set are there to give nice graphics in ANSA, and they differ between the cars. The only colours in the table are the one that can be seen in *figure 15*. The parts included in each PID can be seen in Appendix A.

Table 1 - List of all PID's and its colour for the Mercedes-Benz.

PID name	Colour in figure 15
Exterior_Body_3	Dark purple
External_Parts_2	Dark green
Front_Wheels_2	Light Grey-blue
Gubbe_3	Brown
Helmet_2	Black
Interior_3_	Light purple
Interior_Body_3	Not displayed
Radiator_Outlet	Not displayed
Radiator_Sides	Not displayed
Radiator_inlet_2	Not displayed
Rear_Wheels_2	Yellow-green
Suspension_Front_2	Grey-Beige
Suspension_Rear_2	Dark red
Vents_1	Purple
Wing_2	Lime green

5.3.3. STAR-CCM+

The cleaned geometries of the cars from ANSA were then exported as (.stl) files to STAR-CCM+ where STAR-CCM+ reads them as a surface mesh. The surface mesh made in ANSA is a good mesh for preserving the curves, but it is not suitable for generating a volume mesh to run CFD-simulations. Therefore a new surface mesh was created in STAR-CCM+ according to the user's settings. Before this operation is performed, settings for the following sections have to be made:

- Create a wind tunnel and refinement boxes
- Assign parts to regions
- Set mesh model and cell sizes
- Repair surfaces and generate surface mesh with surface wrapper
- Create a volume mesh
- Set boundary conditions, initial conditions and physics models
- Set solver settings
- Run the simulation

Settings for an Optimal Mesh

To receive the right amount of simulations in time, the mesh settings were of great importance. To save computational power it is important to avoid wasting cells, in other words, not to use a too fine mesh in areas where it is not needed. Since the flow around the vehicle will vary a lot, a mesh with different cell sizes is desirable.

The *wind tunnel* was created according to recommendations from the external aerodynamic course for both cars. With the wind tunnel inlet five body lengths upstream, outlet ten body lengths downstream, five body lengths in width and roof three characteristic heights from the centre of the car. For both vehicles the wind tunnel was set to 68 m in length, 5 m in height and 14 m in width.

Refinement boxes are tools used to mark a volume where cell growth is prevented. For these boxes, customized mesh conditions and values are set. The boxes were used where the flow is particularly turbulent, in this case around both the front and the rear wheels, and another less fine around the whole car. The refinement box settings were the same for both vehicles and can be seen in *figure 16*, which illustrates the refinement boxes after the volume mesh had been generated.

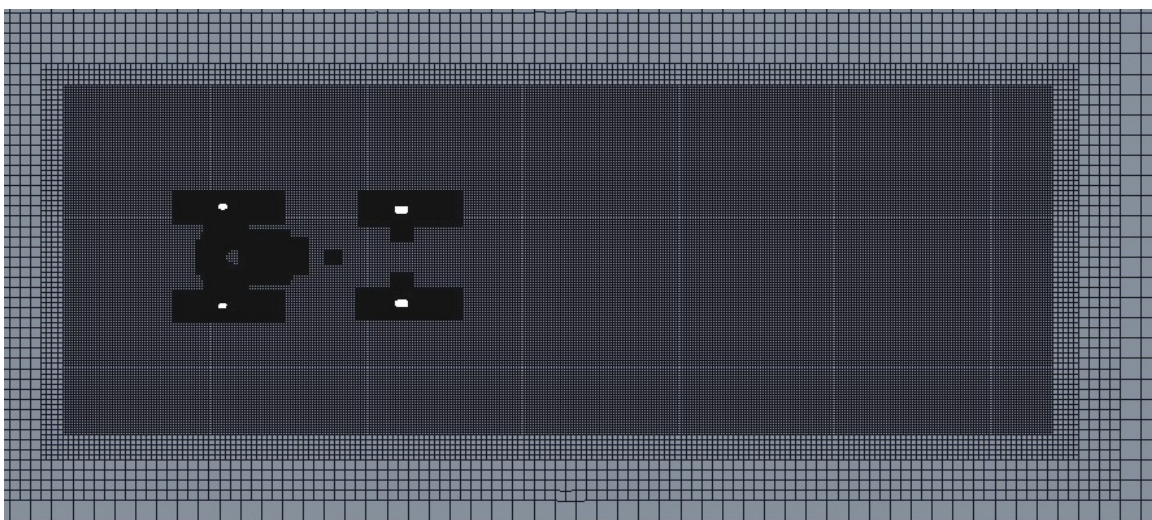


Figure 16 - Illustration of refinement boxes around the wheels and the vehicle.

The PIDs from ANSA, as earlier mentioned, were imported into STAR-CCM+ as one part with different surfaces representing each PID. A separate part with the radiator was also imported with surfaces representing each PID concerning the radiator. The whole vehicle and the radiator were then assigned to two different regions where the first region was merged with the wind tunnel. By using the already defined numbers, of the PIDs names set in ANSA, the settings for each surface were easily made. The settings for each number of the PIDs presented in *table 1, page 20*, can be seen in *table 2*. Number 4 in table below, represents the setting for the wind tunnel.

Prism layers were also used to refine the mesh close to the boundary of the surface. Prism layers are prisms extrapolated from the surface in layers, used to help capture the boundary physics.

Table 2 - Settings for the different PIDs.

PID number	Absolute minimum size	Absolute target size
1	0.002 m	0.004 m
2	0.004 m	0.008 m
3	0.014 m	0.020 m
4	0.200 m	0.400 m

Creating the Mesh

A volume mesh is built on top of a surface mesh, therefore a good surface mesh is required. To create a surface mesh a tool called *surface wrapper* was used. The surface wrapper creates a continuous closed volume by searching for all the surfaces that will be in contact with the outside air and creates a new surface from this data. If there are gaps and holes smaller than a certain reference value they will be closed, this reference value can differ for different PIDs and this depends on the mesh settings for each PID. The surface was then reconstructed with the settings regarding cell sizes as earlier shown in *table 2*. To explain this in a more simplified way, imagine a plastic bag around a geometry and then remove the inside air, the plastic bag will then wrap around all the features of the geometry and the new geometry is represented by the plastic bag.

In STAR-CCM+, there are different kinds of volume elements used to simulate the flow. A common volume element in external aerodynamic simulations is the *trimmer mesh*, which is a cubic volume element. The trimmer mesh works well in these kinds of simulations because the flow is well aligned with the mesh. Therefore the trimmer mesh is the model of choice. Three prism layers were used to accurately capture the boundary physics without using too many cells leading to increased simulation times.

In *figure 17, page 23*, a vertical plane cutting the volume mesh of the Auto Union in half can be seen. Here different sizes of the trimmer mesh due to refinement boxes and region settings can be seen. The mesh has a finer grade closer to the car and around the surfaces with complex geometry. If looking closely, the three layer prisms can be seen on each side of the exterior body.

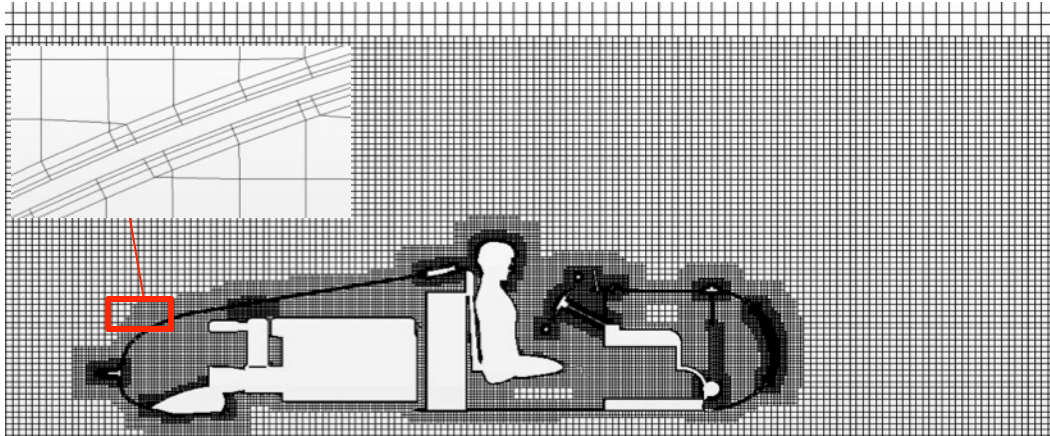


Figure 17 - Plane cutting through the Volume mesh of the Auto Union in the center.

5.4. Solving

After a well performed pre processing stage was completed, the solving stage was conducted. In this stage the simulations were carried out for both cars at different velocities and angles.

With an accurate volume mesh, the boundary conditions and the initial conditions were set. The following physical models were used in all simulations:

- K-Epsilon Turbulence
- Steady (flow)
- Three Dimensional
- Turbulent
- Reynolds-Averaged Navier -Stokes
- Second order discretization for coupled flow
- Constant density
- Realizable K-Epsilon Two-Layer
- Two layer all y^+ wall treatment
- Gas: Air
- Gradient method: Hybrid Gauss-LSQ

And the solver settings were:

- Coupled Implicit
- K-Epsilon Turbulence
- K-Epsilon Turbulent Viscosity

The different settings depending on what type of simulation presented in the objective can be seen on the next few pages:

5.4.1. Zero-Angles

The first simulation was at constant velocity and all angles set to zero. The inlet boundary condition of the wind tunnel was set to a velocity inlet with the velocity 80 km/h, the outlet was set to a pressure outlet. The side walls and the roof were set to symmetry condition and the ground of the wind tunnel was set as a moving wall with the same velocity as the inlet, to simulate the road as it would be moving under the vehicle. The wheels were also given the moving boundary condition with a velocity to simulate the rotation velocity. The boundary settings used can be seen in *table 3*.

The radiator was set to a porous region. The radiator inlet and the outlet were given boundary conditions as interfaces, which enables air to pass through the surface. By having one individual region for only the radiator, specific resistances in x, y and z direction could be made possible, this represent very well a real radiator, *table 3*.

Table 3 – All the different boundary settings used.

Domain Boundary	Boundary condition
Velocity inlet	Velocity: 80 km/h Turbulent intensity: 0.01 Turbulent viscosity ratio: 10
Pressure outlet	Zero gradient in flow direction for all variables
Walls and roof	Symmetry condition
Floor	Moving wall, velocity: 80 km/h
Model geometry	Wall with no slip condition
Wheels	Rotating with angular velocity Auto Union front wheels: 61.75 rad/s Auto Union rear wheels: 58.76 rad/s Mercedes-Benz front wheels: 59 rad/s Mercedes-Benz rear wheels: 59.96 rad/s
Radiator	Porous inertial resistance ρC : XX: 90 000 kg/m ⁴ YY: 900 kg/m ⁴ ZZ: 90 000 kg/m ⁴ Porous viscous resistance $\frac{\mu}{\alpha}$: XX: 45 000 kg/m ³ -s YY: 450 kg/m ³ -s ZZ: 45 000 kg/m ³ -s

5.4.2. Varying Yaw Angle

In reality the flow is not always coming straight in front of the car, e.g. side wind, changing lanes or high speed turns, this must be taken in consideration when evaluating a car's aerodynamical performance. The wind was considered as two-dimensional, with one component perpendicular to the side, and the other one parallel to the side. The resultant of the two components plus the cars traveling speed gives the total relative wind speed and direction. The angle between relative wind direction and the cars direction is called the yaw angle. The effect of the head or tail wind causes changes in drag and lift forces the same way as a corresponding speed of change by the car would have had. The wind perpendicular to the side does also have an effect on drag and lift forces despite that the wind speed in the direction of the car is the same.

To calculate the forces that affect the vehicle with a varying yaw angle, some changes had to be done in the settings. There are a lot of ways to visualize a vehicle driving with a yaw angle, in this project a method by changing the wind tunnel and the refinement boxes were used.

First the wind tunnel and the refinement boxes were enlarged both behind the car and on the side downwind to the flow. It was done to make the mesh finer diagonally behind the vehicle since the wake was predicted to develop there. The wind tunnel must be constructed with a width wide enough so that the wind affecting the car exits through the pressure outlet. The result of the volume mesh around the car can be seen in *figure 18*.

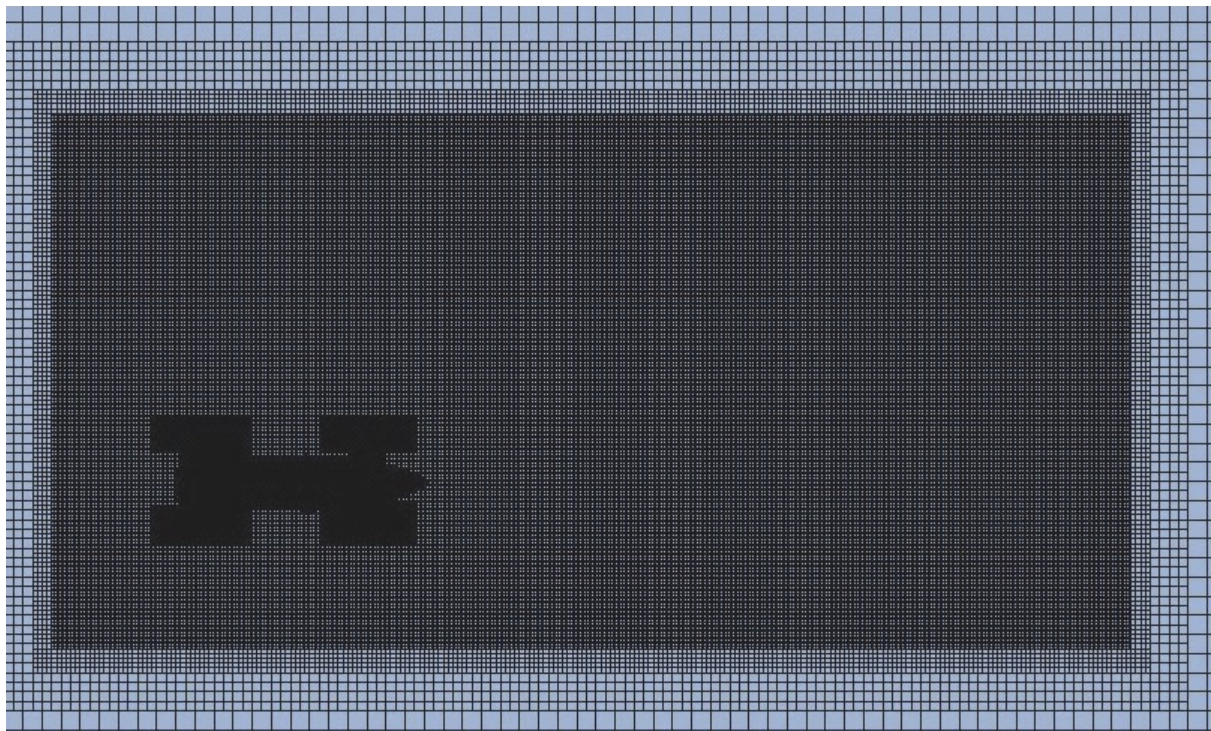


Figure 18 - Volume mesh for varying yaw angle on the Mercedes-Benz.

Secondly, the sides of the wind tunnel were changed into velocity inlets and the direction of the flow was redirected so the flow represented a wind flow from the side whilst the vehicle was moving forward with velocity 80 km/h. The simulation was done for 5, 10, 15 and 20 degrees of the yaw angle, and the directions and the velocity for the different cases can be seen in *table 4*, *page 26*. Otherwise no changes were made with the settings, and the same boundary conditions were used for both vehicles.

Table 4 - Boundary conditions for varying yaw conditions.

Domain Boundary	Boundary condition
Velocity inlet:	
• 5°:	Velocity: 80,30 km/h Direction: [-0,087; 1,0; 0,0]
• 10°:	Velocity: 81,23 km/h Direction: [-0,176; 1,0; 0,0]
• 15°:	Velocity: 82,82 km/h Direction: [-0,268; 1,0; 0,0]
• 20°:	Velocity: 85,13 km/h Direction: [-0,364; 1,0; 0,0]

5.4.3. Varying Pitch Angle

To simulate cases where the vehicle is accelerating or braking, different pitch angles are evaluated. The main reason for doing these simulations is to see how lift and drag changes when the body diverts from the normal position.

The size of the wind tunnel and the refinement boxes in these simulations is the same as in the zero pitch simulation, so the results can be compared fairly. The settings in general are also the same, the only difference is the geometry change.

To achieve the right geometries the car is tilted in ANSA. Four simulations have been executed, two and three degrees for accelerating and the same for braking, *figure 19*. To accomplish this, the body of the cars were lowered in the rear and raised in the front, and vice versa depending on the case. The wheels remained at the same height and the suspension parts morphed to fit both the car body and the wheels.

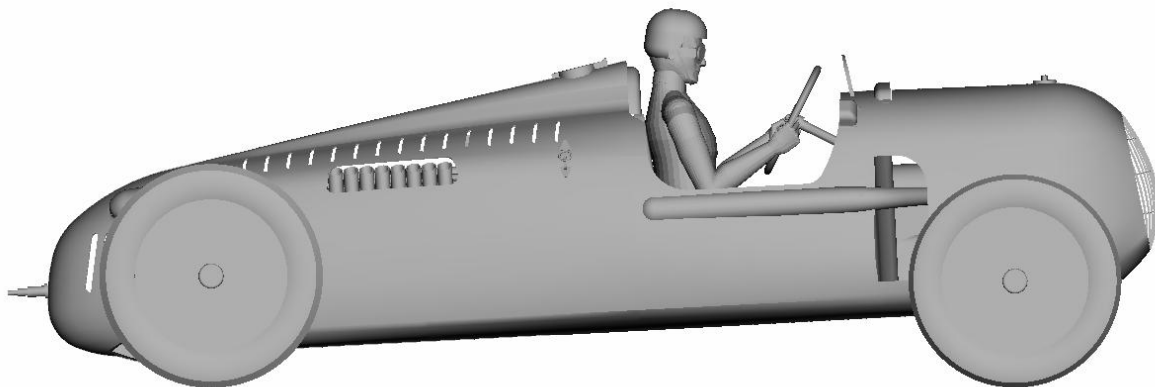


Figure 19 - Illustrating a 3° pitch angle on the Auto Union.

5.4.4. Varying Roll Angle

Lastly, the simulations were made with a varying roll angle and a constant velocity of 80 km/h. To visualize this, some changes had to be done in ANSA before importing the car into STAR-CCM+.

The original vehicle previously imported into STAR-CCM+ was opened in ANSA, and here the goal was to roll the vehicle two and six degrees to the left. By deselecting the four wheels and the suspensions, the rest of the vehicle could be rotated to the desired angle. With this done the vehicle had a rolled middle part that was not connected to the wheels and the suspensions. Therefore, the suspension had to be morphed into the right position for each wheel. The result of the ANSA file for the Mercedes-Benz can be seen in *figure 20*. The new ANSA file was then imported into STAR-CCM+ where the original settings used in zero angle simulation could be used.

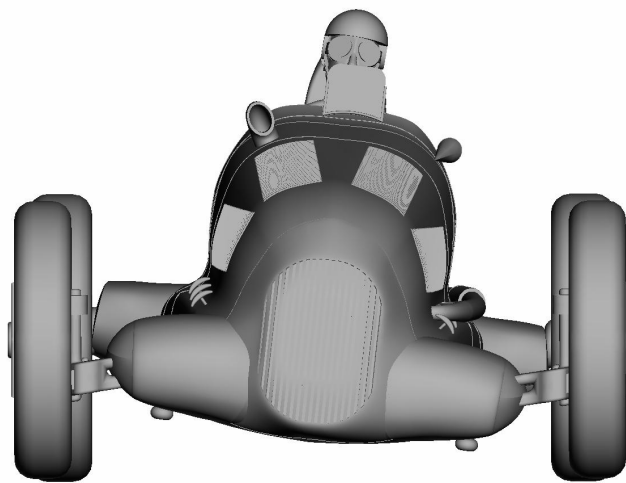


Figure 20 – Mercedes-Benz with a 6° roll to the left.

5.5. Post Processing

After the simulations were solved, analysing the results and the post processing were carried out in STAR-CCM+. The main reason for post processing is to analyse the results, to determine the aerodynamic properties and to understand the flow structure.

5.5.1. Scenes

Most of the time spent on post processing was creating and analysing different scenes. There is a lot of information that can be revealed once the simulations have been solved, the information can then be easily visualized by creating scenes. These scenes are usually isometric views with different cutting sections of the car and can display aerodynamical properties by creating scenes such as streamlines, velocity, iso-surfaces, pressure coefficients, etc. Scenes have the great advantage of being able to describe the aerodynamics on an easy and intuitive way. It is necessary to have this visualizing tool to be able to determine if the results are reasonable or not, and also to understand how different parts affect the flow.

In this project, scenes regarding pressure and velocity are of high interest since they very well visualize how the flow affects the vehicle. Also scenes with the velocity magnitude over different cutting sections of the vehicle were made to visualize how the flow acts both inside and outside the vehicle.

5.5.2. Reports

Post processing cannot only present pictures and animations, it can also present hard fact in terms of numbers, compiled in a report. The most common figures are values like forces and moments in different directions of the whole car. If some specific region needs to be analysed, for example the rear wing, this part can easily be isolated, and a report can be generated with only that parts contribution to the downforce. Practically all values of interest are given in the reports. Some specific values such as force on front and rear axle are not given, but can easily be calculated with help of other values such as moment around specific axles, e.g. the axle where the tyres meet the ground. Values given from reports can advantageously be presented in different types of charts.

6. Results

In this section the results from the simulations are presented in tables and graphs. Conclusions and comparisons are also made regarding the aerodynamical properties for both cars. The results are presented and compared for different scenarios such as different speeds, and different yaw, pitch and roll angles. The results are analysed in the section "Analysis of the results" at page 37.

6.1. Zero-Angles

The first simulations to be carried out on both the Auto Union and the Mercedes-Benz were the ones with yaw, pitch and roll angles set to zero, and the velocity set to 80 km/h and 120 km/h. The frontal area of the Mercedes-Benz is $1,222 \text{ m}^2$ and $1,253 \text{ m}^2$ for the Auto Union. From these four simulations both drag and lift forces were calculated and can be seen in *table 5*.

Table 5 - Drag and lift forces and the coefficients for drag and lift on both cars.

Zero-Angles	F_{Drag} [N]	C_D	$C_D A$ [m ²]	F_{Lift} [N]	C_L	$F_{\text{Lift,Front}}$ [N]	$F_{\text{Lift,Rear}}$ [N]
Auto Union							
- 80 km/h	249,9	0,683	0,856	7,4	0,020	64,2	- 56,8
- 120 km/h	557,4	0,678	0,850	10,4	0,013	144,0	- 133,6
Mercedes-Benz							
- 80 km/h	182,1	0,511	0,625	- 14,8	- 0,042	- 4,4	- 10,4
- 120 km/h	407,3	0,508	0,621	5,5	0,007	- 2,9	8,4

The Mercedes-Benz has a lower C_D and has a smaller frontal area compared to the Auto Union, which makes the drag force significantly lower. The Mercedes-Benz has 27% lower drag than the Auto Union, which corresponds to a power difference of 2 hp at 80 km/h. This change may seem small, but bare in mind that the power is proportional to the velocity cubed. The corresponding power difference in 250 km/h would be just over 60 hp. Cars in general can be considered to have a C_D independent of Reynolds number for normal range of cruising speed, and it seems to be the case for these cars as well (Barnard, 2009). C_L cannot be seen as Reynolds number independent and this is in line with results in *table 5*. *Figure 21* illustrates that the drag coefficients are insensitive to velocity and how the drag forces change with velocities.

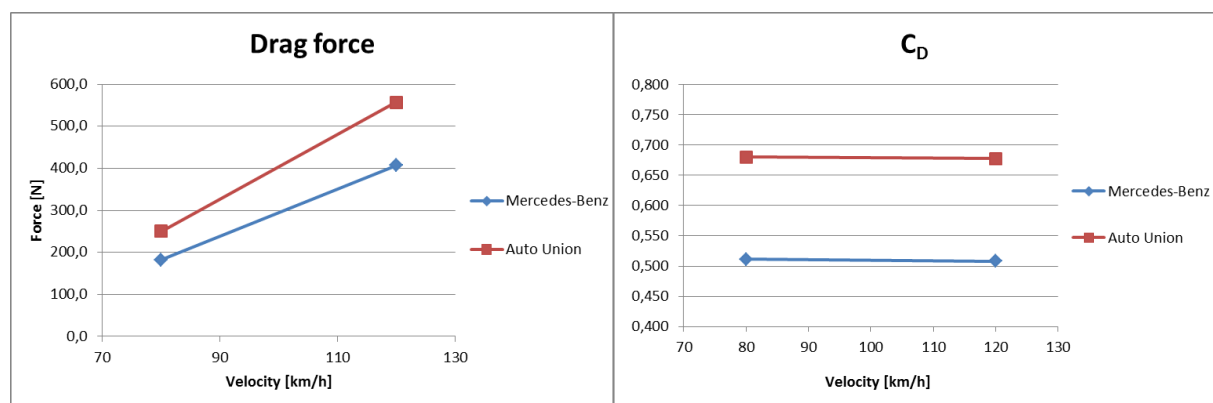


Figure 21 - Drag force and drag coefficient for both cars at no angles.

The Mercedes-Benz has a negative lift force, yet very small, whilst driving in 80 km/h where it is desirable to increase the grip on the road. Whilst driving in 120 km/h the lift force change to become positive yet very small, see *figure 22*. The Auto Union has a slight increase in overall lift force, however the distribution is a bit uneven. The rear downforce is 56,8 N at 80 km/h where 46,2 N comes from the wing. The lift force on the front has the same magnitude, but in opposite direction, *figure 23*. Such an uneven distribution of lift forces might affect the handling of the car. This can result in under steering but no general conclusion from only these results can be drawn.

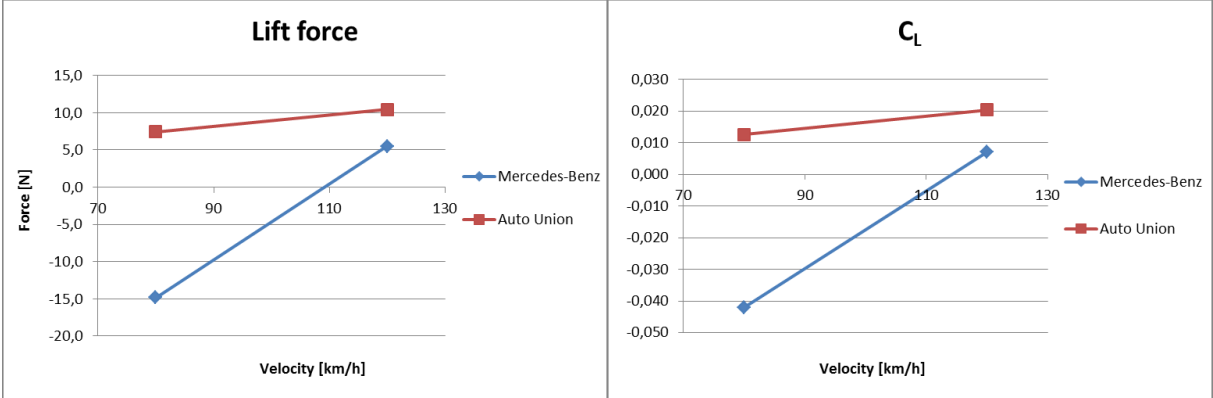


Figure 22 - Lift force and lift coefficient for both cars at no angles.

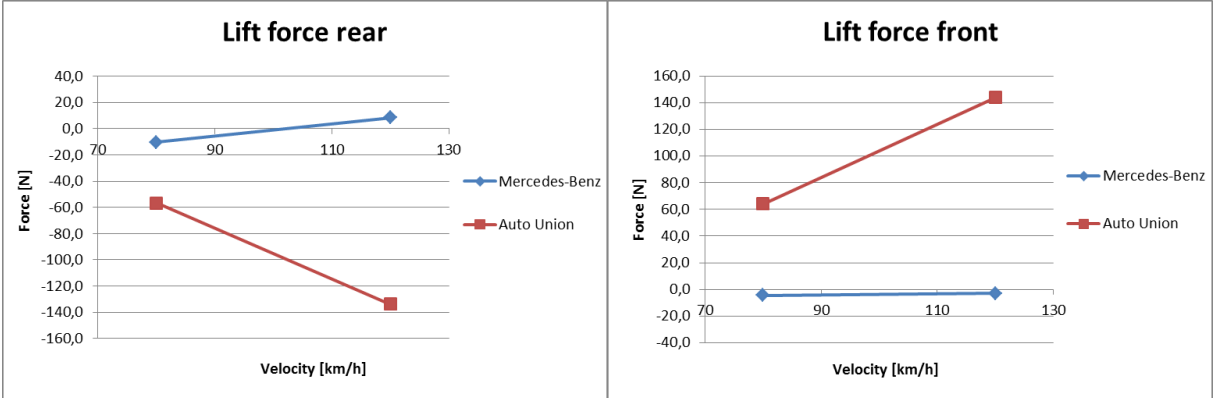


Figure 23 - Distribution of lift force on rear and front axle of the cars.

6.2. Varying Yaw Angle

Table 6 shows the aerodynamical properties of the cars for different yaw angles when driving in 80 km/h. The highest yaw angle tested was 20°, that corresponds to a side wind of 29,12 km/h when driving at 80 km/h. The frontal area in this report is always the projected area normal to the drag of the car, thus, the frontal area is the same as for all yaw angles.

Table 6 - The aerodynamical properties for both cars at different yaw angles and velocity 80 km/h.

Yaw Angle	F_{Drag} [N]	C_D	$C_D A$ [m ²]	F_{Lift} [N]	C_L	$F_{\text{Lift,Front}}$ [N]	$F_{\text{Lift,Rear}}$ [N]	$F_{\text{side,Left}}$ [N]
Auto Union:								
- 0°	249,9	0,683	0,856	7,4	0,020	64,2	- 56,8	- 2,0
- 5°	255,1	0,700	0,877	12,1	- 0,020	60,6	- 48,5	- 69,6
- 10°	262,7	0,720	0,902	- 4,0	- 0,033	56,3	- 60,3	- 155,5
- 15°	291,1	0,797	0,999	- 6,4	- 0,018	60,4	- 66,8	- 235,0
- 20°	318,2	0,870	1,090	-15,3	- 0,042	57,6	- 72,9	- 334,4
Mercedes-Benz:								
- 0°	182,0	0,511	0,624	- 14,8	- 0,042	- 4,4	-10,4	- 8,0
- 5°	182,6	0,513	0,627	- 16,0	- 0,045	5,1	- 20,1	- 81,8
- 10°	191,2	0,537	0,656	- 12,1	- 0,034	8,8	- 20,9	- 168,6
- 15°	198,3	0,557	0,681	- 29,1	- 0,082	8,0	- 37,1	- 270,1
- 20°	211,2	0,721	0,721	- 70,3	- 0,197	- 3,7	- 66,6	- 362,6

The Mercedes-Benz has lower drag and C_D values for all yaw angles. The Auto Union's drag is 51% higher compared to the Mercedes-Benz in 20° yaw angle. That difference corresponds to 4,4 hp at 80 km/h. Figure 24 shows the drag force and the C_D values for both cars. A clear trend can be seen in both charts; the C_D values and the forces increase when the yaw angle increase.

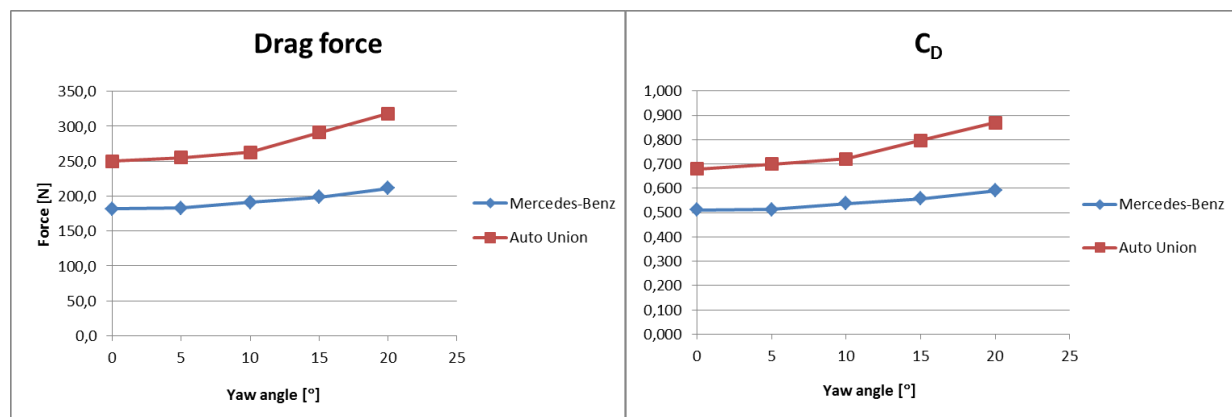


Figure 24 - Drag force and drag coefficient for both cars at varying yaw angles.

In *figure 25* it can be seen that the lift forces are decreasing with higher yaw angles, but a small increase can initially occur. The C_L plot looks the same because the frontal area and the velocity of the car is the same. The lift forces on the front and rear axle can be seen in *figure 26*. The Auto Union has positive front lift force for all yaw angles, and the Mercedes-Benz altering between lift force and downforce on the front axle. For the rear axle, both the Auto Union and the Mercedes-Benz have downforce.

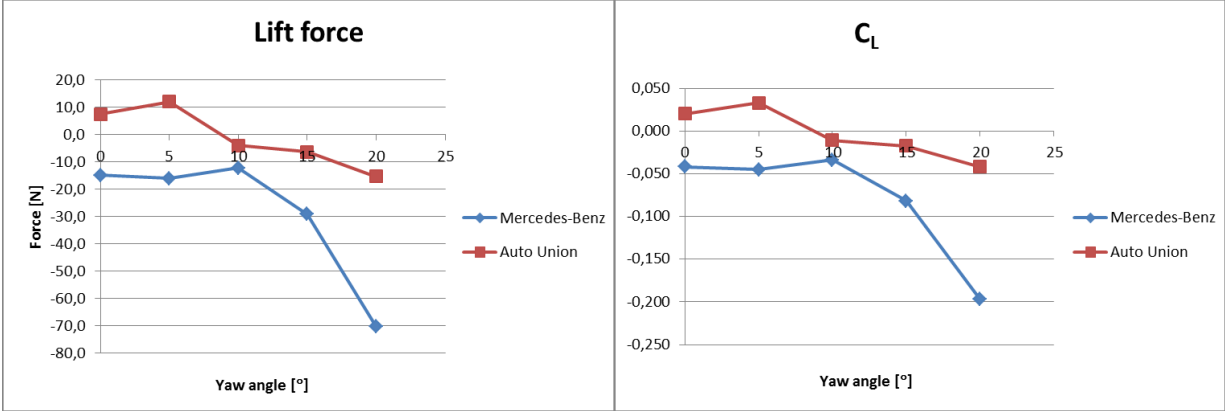


Figure 25- Lift force and lift coefficient for both cars at varying yaw angles.

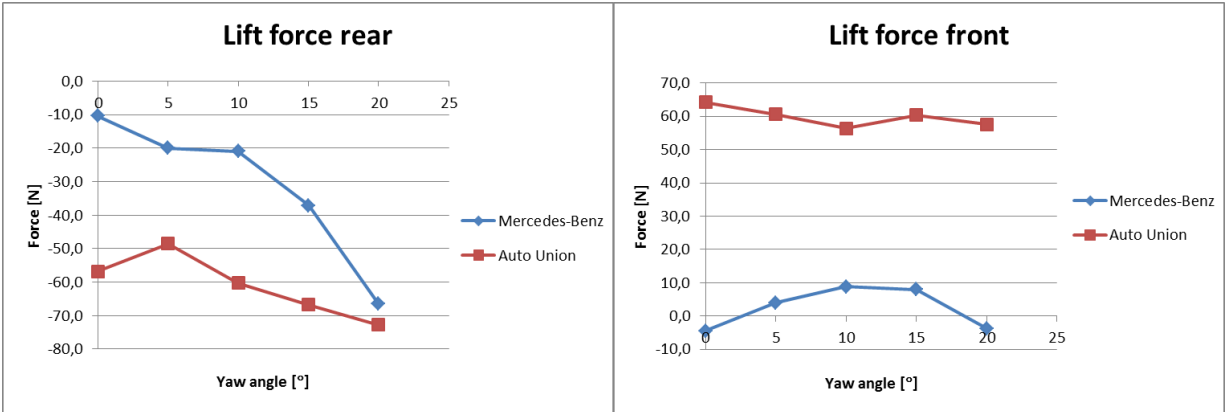


Figure 26 - Distribution of lift force on rear and front axle of the cars.

6.3. Varying Pitch Angle

The following simulations were done with a constant velocity of 80 km/h and with four different pitch angles. The pitch angles correspond to accelerating with positive pitch angles and braking with negative pitch angles. *Table 7* shows the results of the simulations, the frontal area that has been used is the area projected perpendicular to the flow at each pitch angle. This means that the frontal area changes depending on how much the car is pitched.

Table 7 – The aerodynamical properties for both cars at different pitch angles with velocity set to 80 km/h.

	F_{Drag} [N]	C_D	$C_D A$ [m ²]	F_{Lift} [N]	C_L	$F_{\text{Lift,Front}}$ [N]	$F_{\text{Lift,Rear}}$ [N]
Auto Union:							
- Braking - 3°	244,4	0,674	0,840	5,6	0,015	33,0	- 27,7
- Braking - 2°	243,2	0,672	0,835	14,9	0,041	51,1	- 36,2
- 0°	249,9	0,683	0,856	7,4	0,020	64,2	- 56,8
- Accelerating 2°	249,2	0,650	0,854	28,6	0,075	79,7	- 51,1
- Accelerating 3°	257,2	0,654	0,883	34,5	0,088	87,7	- 53,2
Mercedes-Benz:							
- Braking - 3°	184,4	0,462	0,633	- 58,3	- 0,146	- 60,4	2,1
- Braking - 2°	182,8	0,483	0,628	- 29,9	- 0,078	- 32,2	2,4
- 0°	182,0	0,510	0,620	- 14,8	- 0,040	- 4,4	- 10,4
- Accelerating 2°	180,7	0,520	0,620	- 9,0	- 0,026	21,2	- 30,2
- Accelerating 3°	186,1	0,527	0,640	2,5	0,007	34,5	- 32,0

As the cars are pitching, one can see small magnitude changes in drag force. For the Auto Union, a positive three-degree pitch (accelerating) results in a 2.9 % increase of drag, and a negative three-degree pitch (braking) result in 2.2 % decrease of drag. For the same cases on the Mercedes-Benz the accelerating causes a 2.3 % increase and the braking causes a 1.3 % increase of drag. As seen in *figure 27* the Auto Union has significantly higher drag forces and C_D than the Mercedes-Benz through the entire spectrum of pitch angles. This means that the Auto Union must compensate with more engine power to maintain the same speed as the Mercedes-Benz. There is, however, one advantage for the Auto Union with negative pitch (braking), higher drag will help the car to slow down.

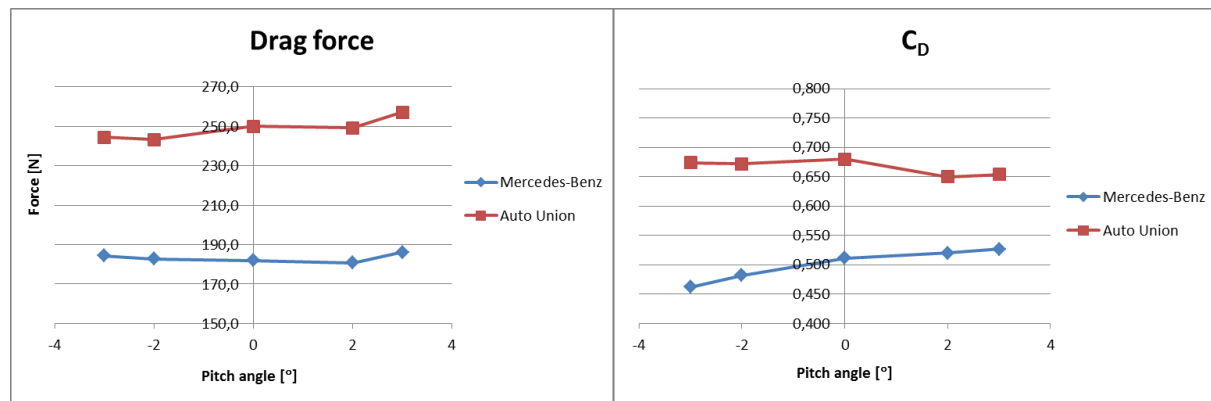


Figure 27 - Drag force and drag coefficient for both cars at varying pitch angles.

To prevent the tyres from losing grip when for example taking corners at high speed, it is important to maintain a high normal force between the rear tyres and the ground (both cars had rear wheel drive). It is achieved through negative lift force on the rear axle. In *figure 29* it can be seen that the Auto Union has a greater downforce on the rear axle compared to the Mercedes-Benz. On the other hand it is visible that the Auto Union has a greater lift force on the front than the Mercedes-Benz, which can make the car unstable.

When braking and the car pitches to a negative angle, it is important to maintain a downforce since the fully developed friction force is directly proportional to the normal force. As seen in *figure 28*, the lift force for the Mercedes-Benz is increasing as the pitch angle increases, from -3° to 3° . The Auto Union has an unclear trend for that scenario.

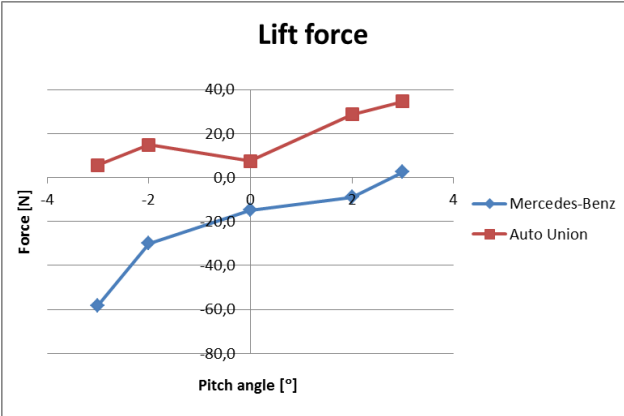


Figure 28 - Lift force for both cars at varying pitch angles.

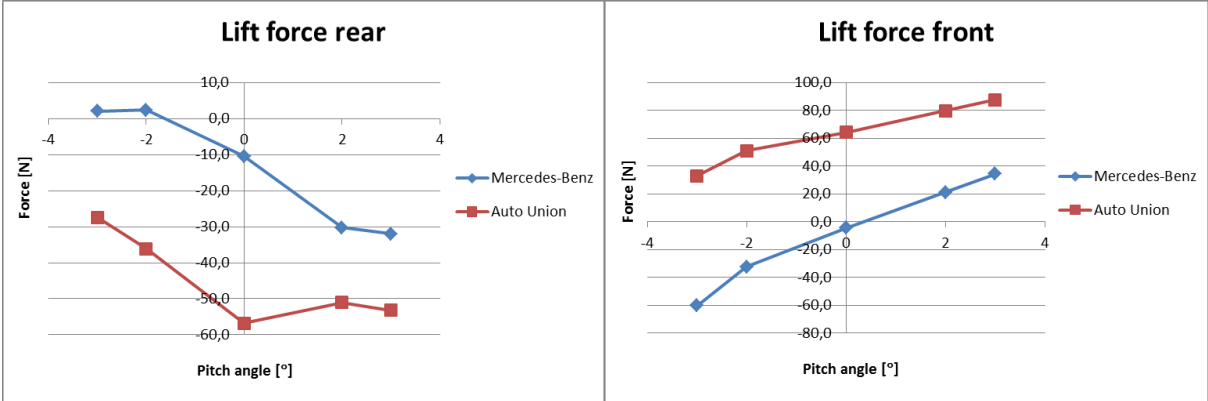


Figure 29 - Distribution of lift force on rear and front axle of the cars.

6.4. Varying Roll Angle

Simulations were also done at two different roll angles for both the Mercedes-Benz and the Auto Union. The simulations are similar to when a car is for example cornering or over taking. However, in this case the wind tunnel is not curved and the tyres are not tilted, as is the general case for cornering simulations. The frontal area used for both cars are the same as for the zero angles simulations, since the difference of the exposed suspension between the two geometries are negligible.

The cars are considered symmetrical, hence it does not matter which way they are rolled, the results shown in this report comes from simulations where the cars were rolled to the left (i.e. taking a right turn). The driving speed was set to 80 km/h. Results of these roll simulations can be seen in *table 8*. Results from the roll 6° simulation for the Mercedes-Benz are missing, due to problems with convergence of the solution.

Table 8 - The aerodynamic properties for both cars at different roll angles and velocity set to 80 km/h.

		F_{Drag} [N]	C_D	$C_D A$ [m ²]	F_{Lift} [N]	C_L	$F_{\text{Lift,Front}}$ [N]	$F_{\text{Lift,Rear}}$ [N]
Auto Union								
-	0°	249,9	0,683	0,856	7,4	0,020	64,2	- 56,8
-	2°	249,1	0,682	0,855	6,3	0,017	60,6	- 54,3
-	6°	241,2	0,660	0,827	37,6	0,103	68,7	- 31,2
Mercedes-Benz								
-	0°	182,0	0,511	0,625	- 14,8	- 0,042	- 4,4	- 10,4
-	2°	186,1	0,523	0,639	- 10,7	- 0,030	0,1	- 10,8
-	6°	N/A	N/A	N/A	N/A	N/A	N/A	N/A

The Mercedes-Benz has a lower drag force than the Auto Union at the 2° roll angle. The Auto Union gets slightly less drag as the roll angle increases and the Mercedes-Benz gets slightly higher drag when it is rolled 2°, *figure 30*.

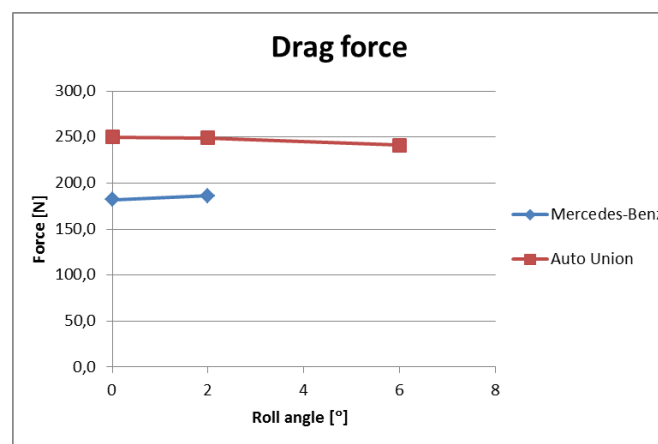


Figure 30 - Drag forces for both cars with varying roll angles.

The lift forces are increasing with roll angle for both cars as seen in *figure 31*. The rear axle of the Auto Union has much more downforce then the Mercedes-Benz. The Auto Union rear axle downforce is reduced to about half when having a roll angle of 6° compared 0°. The change on the rear axle on the Mercedes-Benz is so small that it can be neglected. The front axle of the Auto Union experience lift force at all roll angles. The results show a slight increase in front lift the car is roll 6°. The same tendency is observed on the Mercedes-Benz at 2° roll, but the car is experiencing much less lift on that axle, close to zero. This can be seen in *figure 32*.

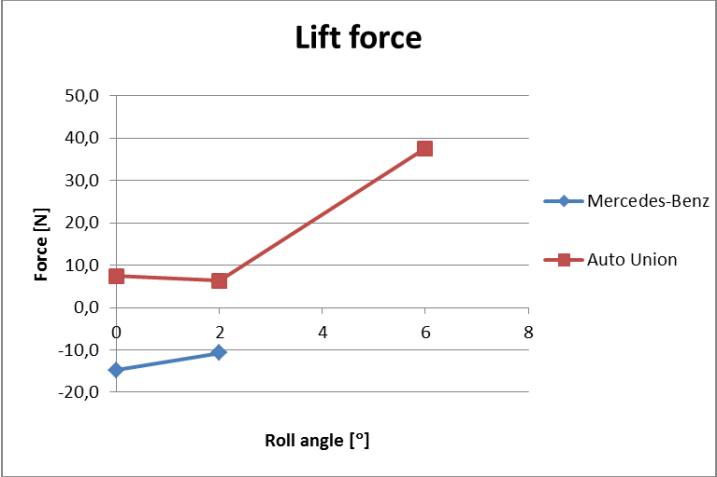


Figure 31- Lift force for both cars at varying roll angles.

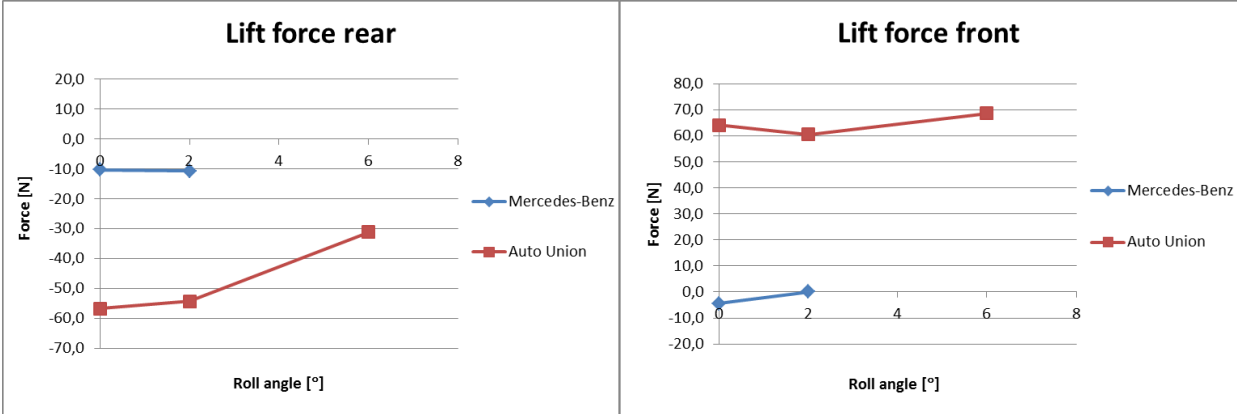


Figure 32 - Distribution of lift force on rear and front axle of the cars.

7. Analysis of the Results

In this section the results from all the simulations are analysed and compared. Conclusions are made regarding magnitude of the different forces by analysing the pressure and velocity that affects the cars.

7.1. Zero-Angles

The zero angle simulations are the most common simulations in CFD and give a good understanding about the general aerodynamic performance. Simulations were run at both 80 km/h and 120 km/h to simulate the average speeds on different tracks used for racing during that period of time (Pritchard, 2008).

7.1.1. Drag

The drag and lift forces are results of pressure differences. Drag by the pressure difference between the front and the rear, and lift by the pressure difference between the top and the bottom of the car. High pressure relates to low speed and vice versa through the Bernoulli equation explained in the theory section, *page 7*. There are different kinds of drag sources but the most prominent one is form drag, also known as pressure drag (Barnard, 2009). Form drag can also be generated through separations, which cause energy losses and reduced speeds that extend far behind the vehicle. These speed reductions seen behind the cars are called wakes (Katz, 1995).

From *table 5, page 29*, in the results it can be seen that the Auto Union has significantly higher drag forces than the Mercedes-Benz. Since the drag is mostly due to form drag the wake is a big contributor to the total drag. Hence the wake from the Mercedes-Benz ought to be smaller than the Auto Union, which can be seen in *figure 33*.

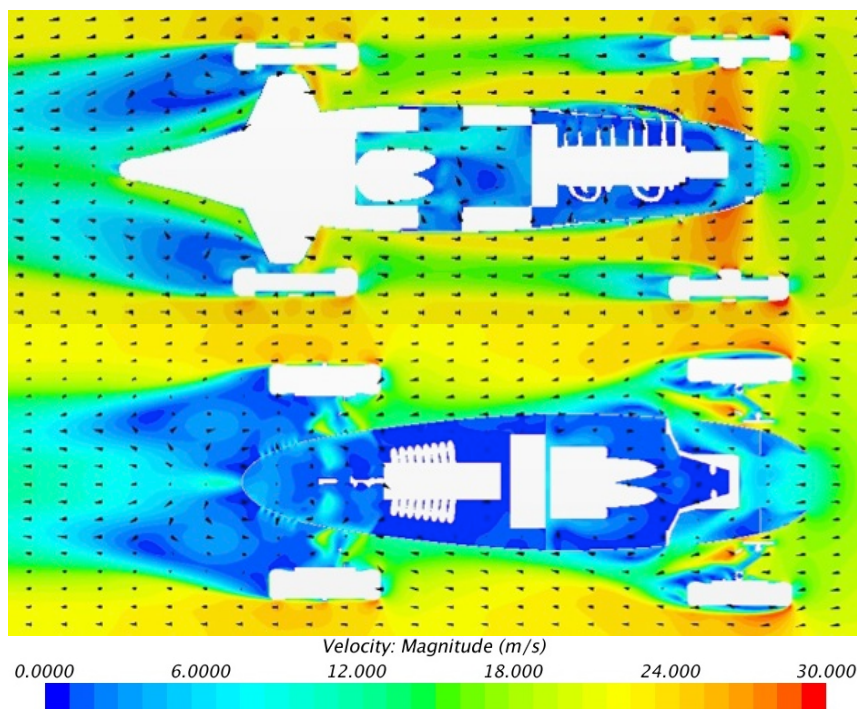


Figure 33 - A horizontal plane just above the rear wheel axle on both the Mercedes-Benz (top) and the Auto Union (bottom).

The flow velocity underneath the Auto Union and the Mercedes-Benz differ a lot, which is seen in *figure 34*. The reason for this difference in velocity could be due to a separation, just behind and below the radiator on the Auto Union, *figure 35*, which reduces the speed all along the undercarriage through the swirls created from this separation. The separation bubble is produced by the air vent beneath the radiator, since the air vent lets air out in an almost perpendicular angle towards the surface of the exterior body, the velocity gradient changes in such a way that the flow becomes detached or separated. The low air speed is then responsible for the big wake at the rear of the Auto Union compared to the Mercedes-Benz.

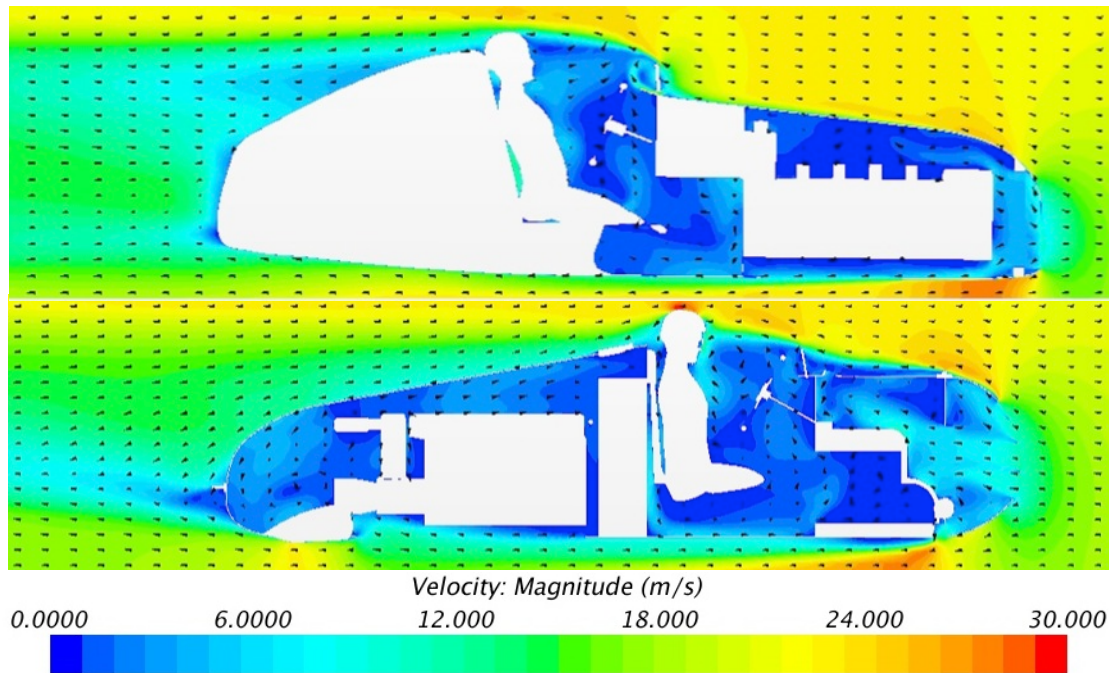


Figure 34 - A vertical plane through the centre of both the Mercedes-Benz (top) and the Auto Union (bottom) displaying the speed of the air around it.

In *figure 35* and *figure 36*, *page 39* an iso-surface on both cars can be seen. The iso-surface shows where the flow is losing energy due to separation and recirculation of the flow. In other words, inside the iso-surface the flow is separated. In *figure 35* the energy loss due to separation around the air vents for both cars can be seen.

The Mercedes-Benz has air vents on the bottom side, but smaller and placed after the radiator. This means that the speed of the air and the mass flow passing through the vents is lower, thus a smaller separation and a higher percentage of attached flow along the undercarriage. Since the biggest part of the flow is attached the overall air speed is higher and this in turn leads to smaller separations at the rear, which equals less drag compared to the Auto Union.

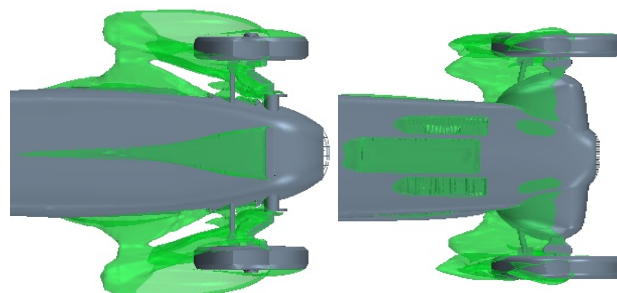


Figure 35 - Iso-surface showing separations on the bottom side on the Auto Union (left) and the Mercedes-Benz (right).

As seen in *figure 36*, the Auto Union has much more energy loss at the rear, which also explains the big wake and part of the high drag force. It can also be seen that the Auto Union has a large separation around the front tyres, most likely due to the open suspension instead of a closed suspension like the one on the Mercedes-Benz. The radiator exit on the side of the Auto Union also causes a big separation compared to the Mercedes-Benz, possibly due to the sharp edges of the hole.

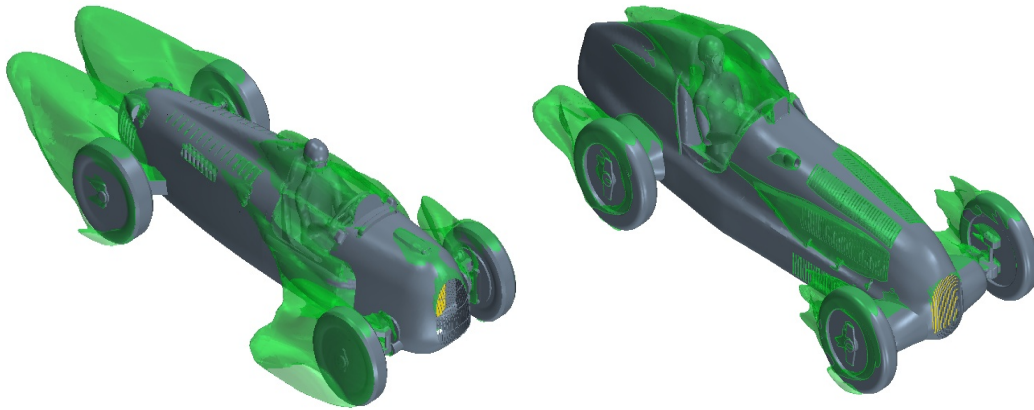


Figure 36 – Iso-surface on the Auto Union (left) and on the Mercedes-Benz (right) showing separations, in other words, where the flow that is losing energy.

7.1.2. Lift

The lift forces are for both cars, as seen in *table 5, page 29*, quite similar. Though looking closer it can be seen that the lift forces on the Auto Union are unevenly distributed between the front and the rear with a lot of down force on the rear axle and a high lift force on the front axle. In principle this means lower pressure underneath the rear and a higher pressure underneath the front.

In *figure 34, page 38*, it can be seen that a part of the above statement is correct. The air flowing underneath the Auto Union splits up into two parts, one part entering the engine bay and another one accelerating underneath the rear wing generating a lower pressure. It is this low pressure that leads to a negative lift force. In *figure 37* it can also be seen that the pressure underneath the rear wing of the Auto Union is significantly lower than above, and generates a large amount of downforce.

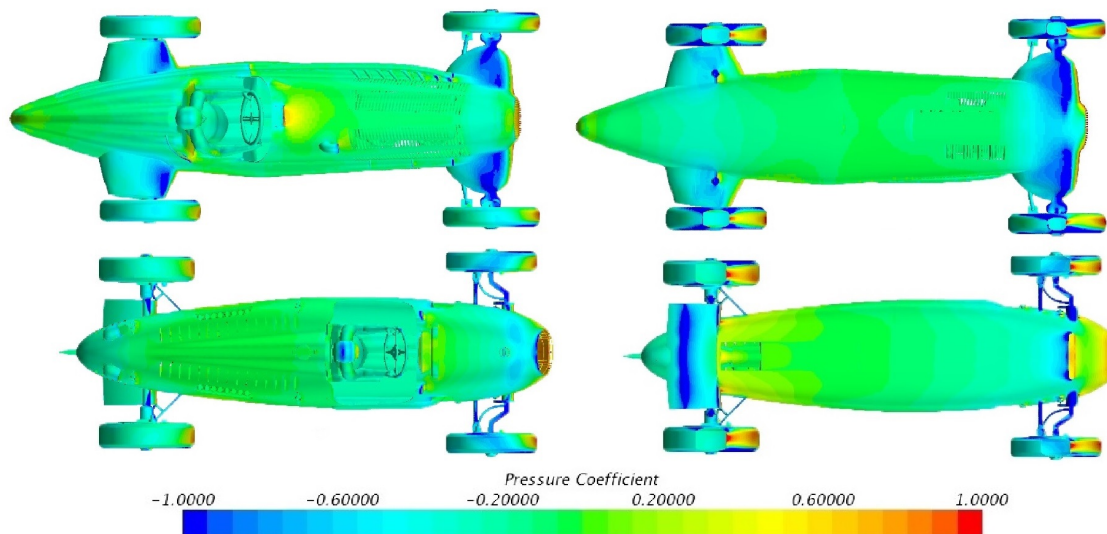


Figure 37 - Pressure coefficient on both vehicles, Mercedes-Benz (top) and Auto Union (bottom).

In *figure 34, page 38*, it can be seen that the hole underneath the Auto Union front axle creates a velocity pointing slightly downwards, which creates a positive lift force in the front. The velocity creates a pressure difference between the top and the bottom of the vehicle with a lower pressure on top. It is also visible that the velocity over the front of the car is high. This velocity prevents the car from achieving a high downforce in the front. These two forces contribute to a total positive lift force. The Mercedes-Benz has, as seen in *figure 37, page 39*, a low pressure both over and under the front axle. This creates a total lift force almost close to zero since the forces generated below and above cancel each other out.

In total, the difference in lift between both cars is small, but the Mercedes-Benz has a bit more downforce. The lift forces are almost the same in total and therefore no major differences between the cars can in this respect be said.

7.1.3. 120 km/h

The results show an increase in drag, which is expected since drag increase to the power of two with speed, as mentioned in section *Zero-Angles under Results, page 29*. Since C_D is almost constant it shows that the simulations follow the theory well. The biggest difference can be seen in lift, where the Auto Union produces much more downforce at the rear and almost equally more lift at the front making the total lift force almost unchanged, but even more unevenly distributed. The Mercedes-Benz downforce at the front is almost unaffected, but at the rear, it changes from downforce to lift force.

7.2. Varying Yaw Angle

In this section the Mercedes-Benz and Auto Union will be analysed separately and in comparison with each other in respect to the results at the different yaw angles for drag and lift. For the comparison, the 20° yaw will be compared to the 0° to be able to see bigger changes. The wind comes from the driver's left hand side in all simulations.

7.2.1. Drag

Both cars shows an increase in drag from 0° to 20° , see *table 6, page 31*. The pressure coefficient is much lower at the rear of the cars with a yaw angle, as seen in *figure 40, page 42, and figure 41, page 42*. The loss in pressure at the rear leads to higher pressure drag. By looking at *figure 38*, it can also see that most of the separation occurs on the side that is not stricken by the crosswind, and on the other side, where the crosswind does hit the cars, the pressure is higher and has a more attached flow.

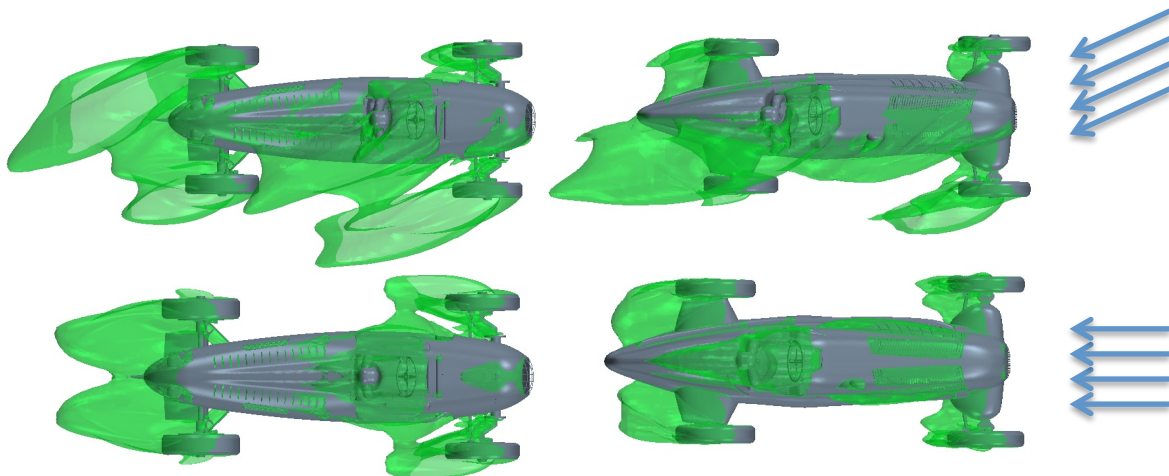


Figure 38 – Iso-surface showing separations on both the Auto Union (left) and the Mercedes-Benz (right) with 20° yaw (top) and 0° (bottom). Blue arrows represent wind direction.

Using an airfoil as an analogy to explain why this happens is somewhat easier. Instead of thinking that the wind comes from a certain angle to the front of the car one can imagine the wind coming straight from the inlet of the tunnel and the car being rotated clockwise for the different yaw angles. As the yaw angle increases, the adverse pressure gradient on the side not exposed to the wind, increases, resulting in earlier separation contributing to a larger drag on the car. The separation along the right hand side effects the wake behind both cars since the flow is not able to reattach to the surface of the narrow cars. As seen in *figure 39*, the flow behind the Auto Union is circulating more and this helps generate a larger wake then on the Mercedes-Benz. (White, 2011)

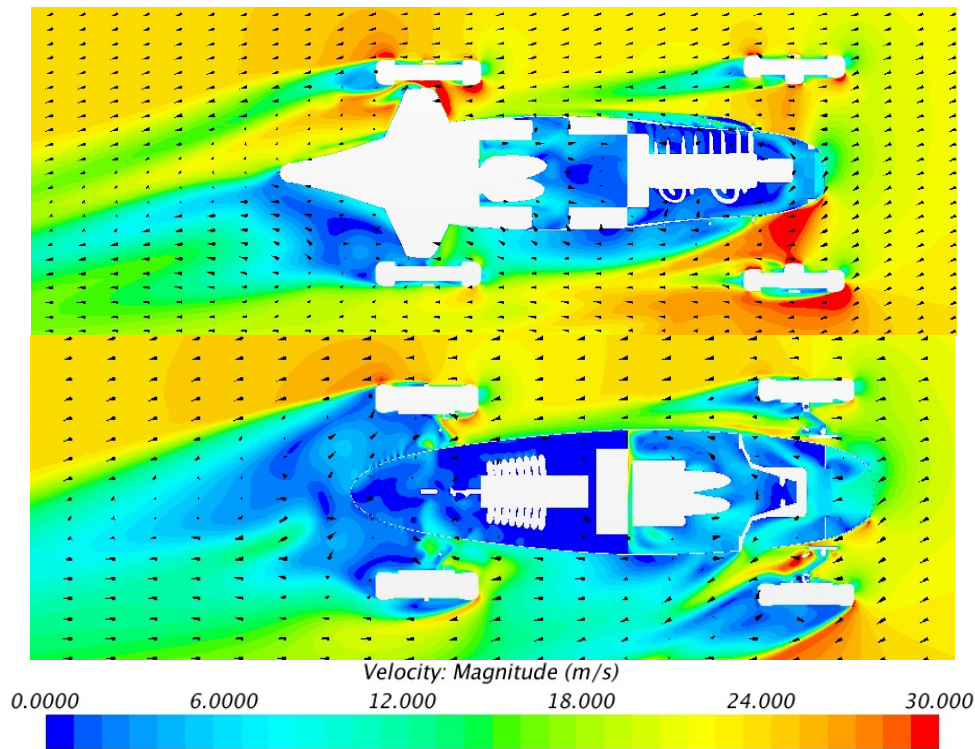


Figure 39 - Velocity plane just above the rear axle on both the Mercedes-Benz (top) and the Auto Union (bottom) at 20° yaw angle displaying wakes and circulations.

Since the speed of the air traveling towards the front of the car is constant, the increase in drag with an increase of yaw angle must be a result of increased C_D , see *table 6, page 31*. In *figure 38, page 40*, it can be seen that the Auto Union has the largest separation, which leads to more drag, which is the case for all yaw angles.

7.2.2. Lift

Figure 40, page 42, also shows that the pressure underneath the Auto Union is lower on yaw 20° compared to yaw 0° at the front of the car. The pressure above the radiator is lower for yaw 20° compared to yaw 0°, and the pressure behind the driver is also lower on yaw 20° compared to 0°. The forces generated by the pressure differences between the top and the bottom on yaw 20° and yaw 0° basically balance each other out, and the lift force remains nearly the same.

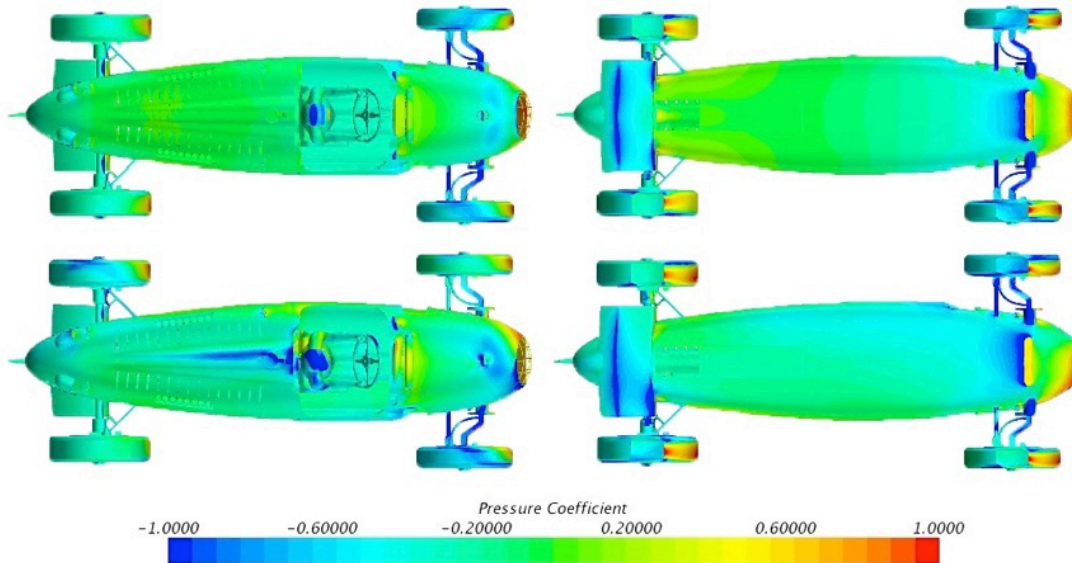


Figure 40 - Pressure coefficient on the Auto Union with 0° yaw angle (top) and 20° yaw angle (bottom). The wind is coming from the driver's left hand side.

For the Mercedes-Benz the pressure over the front suspension at yaw 0° is more evenly distributed compared to yaw 20°, where the low pressure shifts to the right as the yaw angle increases. The lift forces, generated by the pressure, seem to cancel each other, which makes the downforce roughly the same for yaw 20° and yaw 0°.

The rear downforce increases with yaw angle on both cars. The Auto Union has the lowest increase. In *figure 40*, it can be seen that the bottom side of the rear has a bit lower pressure, distributed over a big area. The wing has a bigger pressure drop than the body, and the wing is an important contributor to the rear downforce. However, some of this downforce is reduced due to lower pressure on the top as well.

The Mercedes-Benz has much larger increase in rear downforce compared to the Auto Union. In *figure 41* it can be seen that the wing has lower pressure on the Mercedes-Benz left hand side, both on the top and on the bottom view. The pressure is decreased on the undercarriage and distributed over a large area, but the pressure is lower on the top as well, but distributed over a smaller area. The blue and the yellow area by the drivers shoulder seem to cancel each other out.

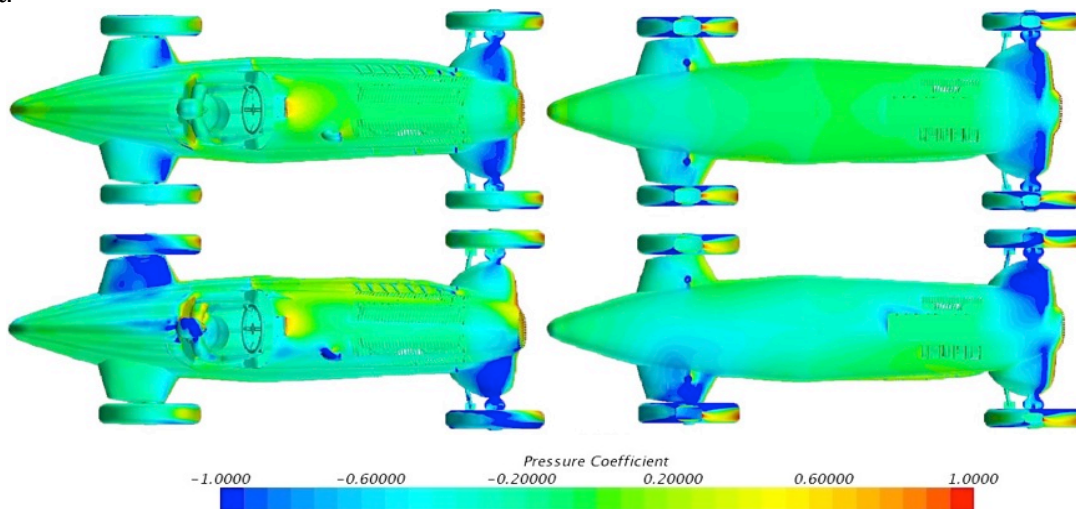


Figure 41 - Pressure coefficient on the Mercedes-Benz with a 0° yaw angle (top) and 20° yaw angle (bottom). The wind is coming from the driver's left hand side.

7.3. Varying Pitch Angle

The purpose of this chapter is to analyse the pitch results and draw conclusions on the results from the previous section *Results*, page 29. Comparison between both cars will also be presented and explained.

7.3.1. Drag

The change in drag force due to a changed pitch angle is for both cars very small. The trend for the Auto Union is however that positive pitch equals less drag and vice versa. For the Mercedes-Benz the trend is almost the opposite, negative pitch equals less drag, and can partially be explained by *figure 42*.

As mentioned before a lot of the total drag can be explained by how many, and how big the energy losses are on each car. Energy losses are areas that cause separations and recirculations of the flow. While a flow is separated or detached energy is lost, i.e. if a separation reattaches the loss of energy will be reduced. (Barnard, 2009)

With a negative pitch angle, the curved backside of the Mercedes-Benz helps the separated flow caused by the windshield to reattach. The reattached flow makes the separation smaller, and this equals less drag. It is also the curved backside that is generating more drag in the positive pitch angle, because in this case it prevents the flows ability to reattach and causes a bigger separation, leading to an increase in drag.

For the Auto Union it is visible that the separation behind the rear is smaller for the positive pitch angle then for both the negative pitch angle and the zero angle. Separation around the front tyre is also less for a positive pitch angle. Both of these smaller separations will lead to less drag and explains the given results.

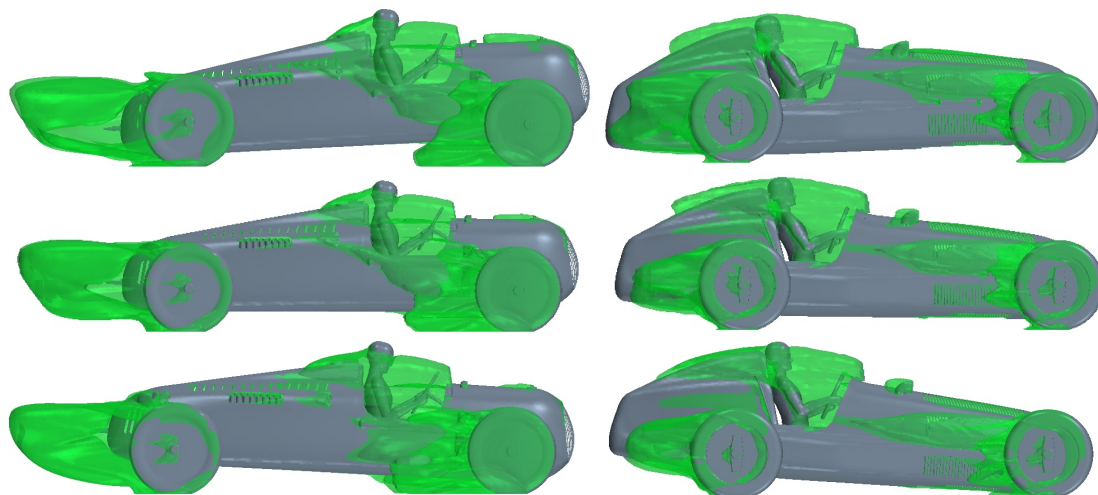


Figure 42 - Iso-surfaces on the Auto Union (left) and the Mercedes-Benz (right), with different pitch angles, positive 3° pitch (top), zero pitch (middle) and negative 3° pitch (bottom). Within the iso-surface the flow is losing energy.

7.3.2. Lift

On the Mercedes-Benz a distinct lift force trend can be seen, the higher the negative pitch angle gets the more the downforce increases, and the higher the positive pitch angle gets the more the downforce decreases. On the Auto Union the same trend can be seen, except for the zero angle pitch, which goes against this trend.

Negative Pitch

With a higher absolute negative pitch angle the ground clearance in the front decreases, this accelerates the velocity under the front axle due to reduced area underneath the front, *figure 43*. This leads to lower pressure and a higher downforce below the front axle. With the same argument the downforce should be lower in the rear with a negative pitch, which the results also show. (Katz, 1995)

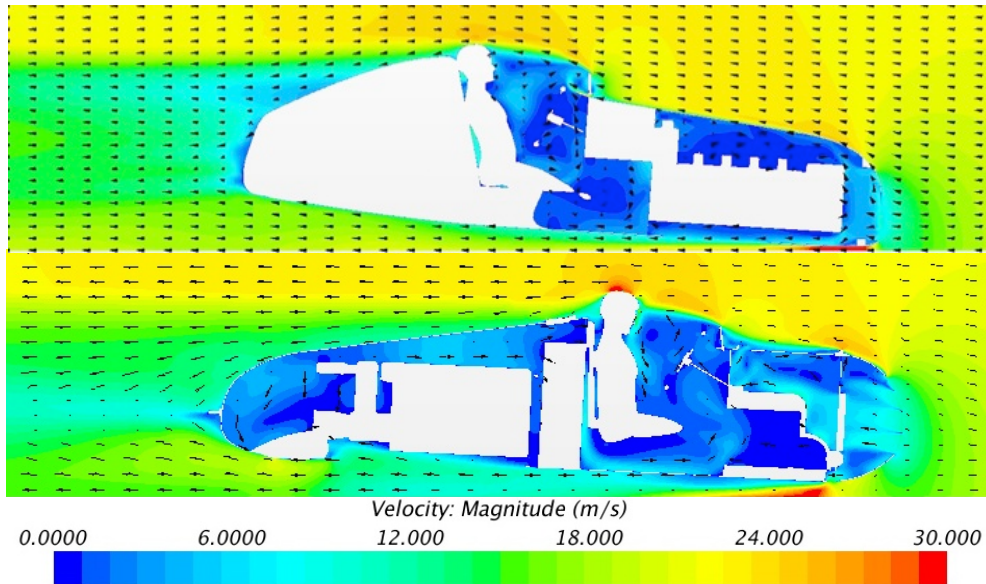


Figure 43 - A vertical plane through the centre of the Mercedes-Benz (top) and the Auto Union (bottom) with a negative pitch angle of 3°.

In *figure 43*, it can be seen that the ground clearance on the Auto Union is higher in the front than on the Mercedes-Benz, this makes the ground effect less beneficial for the Auto Union. But even with the same ground clearance the Mercedes-Benz would still get more downforce in front due to the front wings that surrounds the suspension. This wing increases the area to which a potential low pressure can act upon, see *figure 44, page 45*. The Auto Union's area under the car is smaller than the Mercedes-Benz area, which makes the potential benefit from the ground effect weaker on the Auto Union.

With a negative pitch angle, the Mercedes-Benz gets a positive lift force on the rear axle compared to the Auto Union that still has downforce. These statements can be seen in *figure 44, page 45*, where the Mercedes-Benz has a small low pressure on the top side of the rear wing which causes small positive lift and the Auto Union still has a low pressure on the bottom side which result in negative lift force.

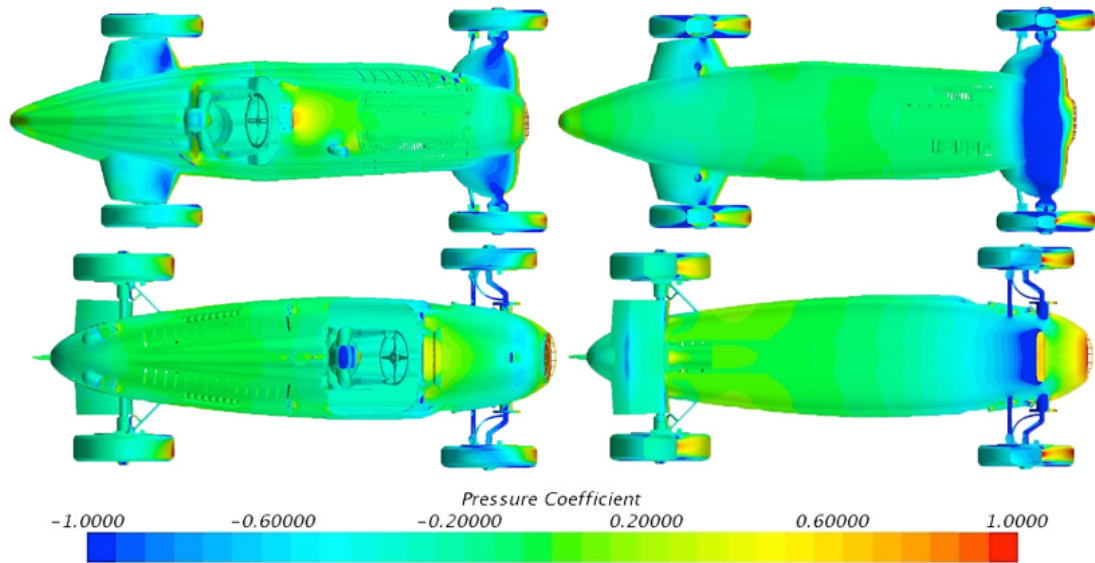


Figure 44 - Pressure Coefficient on the Mercedes-Benz (top) and the Auto Union (bottom) for negative pitch angle (-3°).

Positive Pitch

As explained in the section above, the ground clearance at the rear decreases with a positive pitch angle and vice versa for the front. As a result there should be an increase in downforce for the rear and a drop in downforce for the front. The results support these claims, the only exception is the Auto Union with zero degrees pitch that has the greatest downforce.

The wing on the Auto Union helps generate a much lower pressure on the bottom side compared to the topside, which is the reason for the high downforce on the Auto Union, see *figure 45*, for the pressure coefficients on both cars. On the Mercedes-Benz, the rear wing generates a substantial low pressure on the topside, producing an upward force. This force cancels out part of the forces produced by the low pressure on the bottom side, making the possible downforce on the rear axle considerably lower than what it could be.

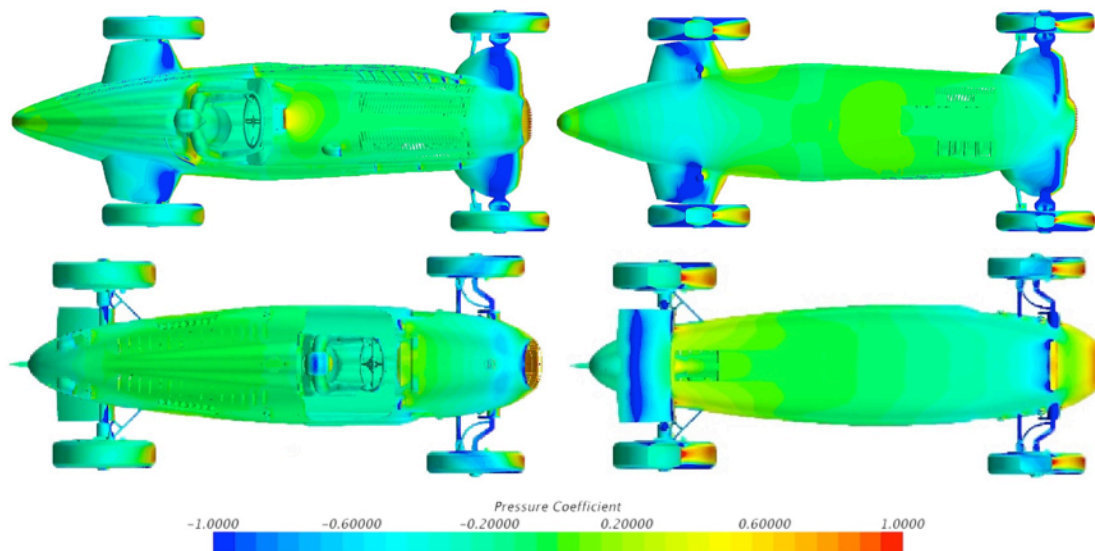


Figure 45 - Pressure coefficient for positive pitch angle with the Mercedes-Benz (top) and the Auto Union (bottom).

7.4. Varying Roll Angle

In this section, the Mercedes-Benz and the Auto Union will be analysed separately and in comparison with each other in respect to the drag and lift results for the different roll angles. The roll angle that is analysed on the Auto Union is the extreme angle, i.e. 6° . The 2° roll angle will be analysed on the Mercedes-Benz since the 6° roll angle is missing. From the driver's point of view, the car is rolled counter clockwise.

7.4.1. Drag

For the Auto Union, the drag due to the 6° roll angle is slightly lower compared to the 0° roll angle. The iso-surfaces, seen in *figure 46*, show that the separations are very similar between the 6° roll and the 0° roll, there are however small differences to be seen. First, the separations at the rear on the 6° roll are shorter and thicker, and they are more asymmetrical, but it is hard to say which separation is the largest. Secondly, the separation by the driver's head is also more asymmetrical. It is not clear which specific area that can explain the small change in drag. Most of the iso-surfaces differ between the roll angles, but the differences are often the shape and not the size. The differences probably give a small contribution to the drag, which add up to a slightly smaller total drag for the Auto Union.

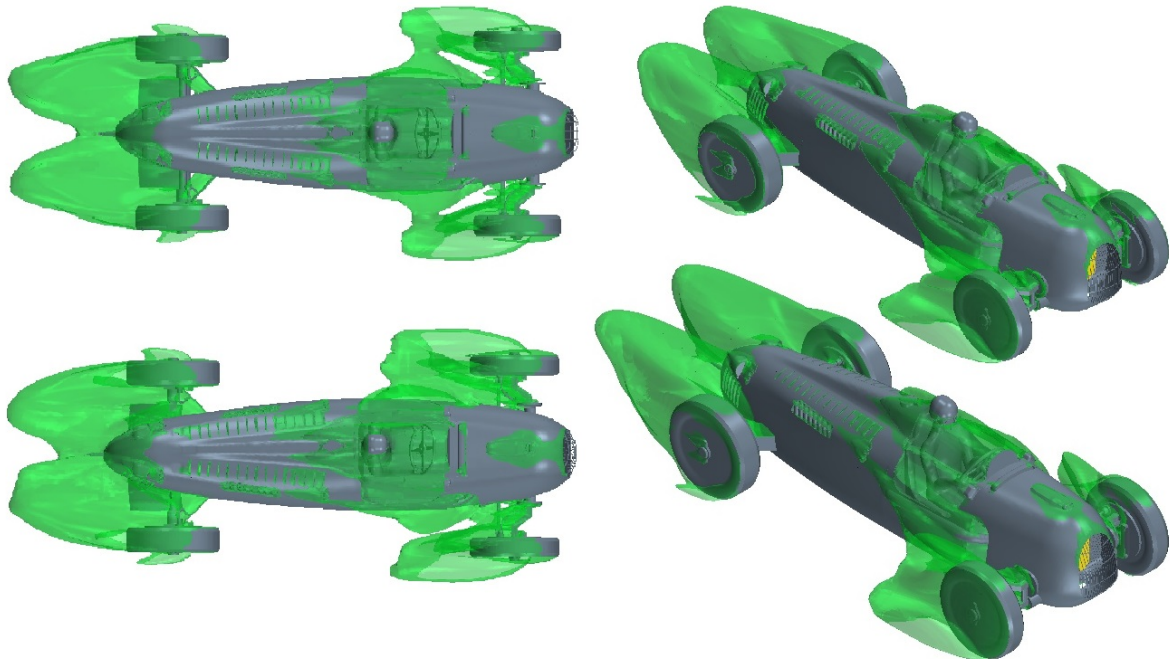


Figure 46- Scene with plotted iso-surfaces showing separations of the Auto Union at 0° (top) and roll 6° (bottom).

The drag is slightly higher for the Mercedes-Benz at 2° roll angle compared to the 0° roll angle. Since the roll angle is smaller for the Mercedes-Benz, it is even harder to see a difference in the separation, *figure 47*, *page 47*. The only clear difference is that the separation behind the rear wheel is a bit larger when the car is rolled, which may be the main contributor to the increased drag.

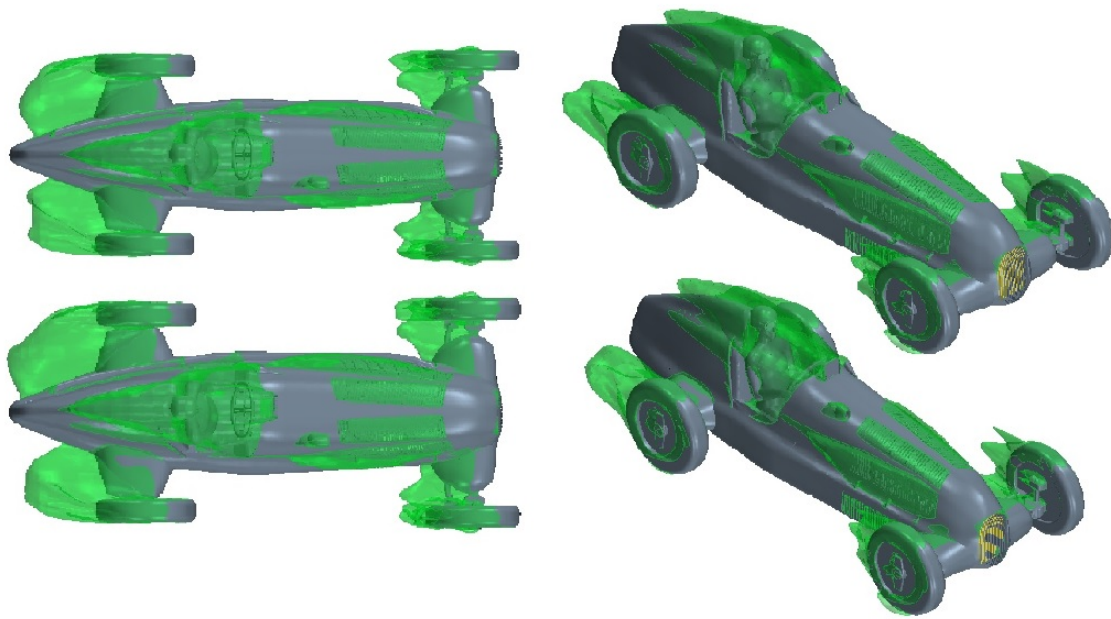


Figure 47 - Scene with plotted iso-surfaces showing separations of the Mercedes-Benz at 0° (top) and roll 2° (bottom).

7.4.2. Lift

The rear downforce is decreasing as the roll angle increases for the Auto Union. The difference in rear downforce is however small, -25,6 N. As seen in *figure 48*, which shows the pressure coefficient on the Auto Union, the pictures are almost identical between the roll angles. The most significant difference between the roll angles is that the blue line under the wing, at the rear, differs in width. The line is much thinner for the 6° roll angle, suggesting that the change of pressure on the wing is the reason for less downforce. The lift reports from the simulations confirm this and show that the wing is responsible for the loss of 20,3 N in downforce. The front lift force on the Auto Union is pretty much the same regardless of roll angle, the difference between 0° and 6° is only 4,5 N. The pressure differences in the front between the roll angles are also almost equally distributed, no difference can be seen with the naked eye in that area in *figure 48*.

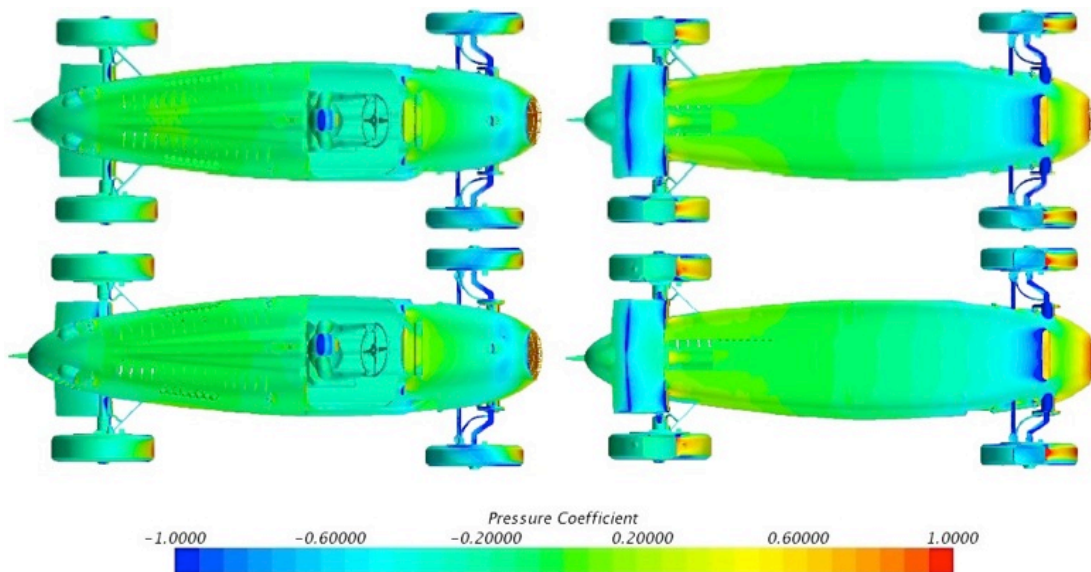


Figure 48- Pressure coefficient on the Auto Union for 0° roll (top) and 6° roll (bottom).

The lift force on the Mercedes-Benz is increasing when it is rolled. Practically all change occurs at the front section. As seen in *figure 49*, the pressure coefficients look very alike between the two roll angles, but there are some minor differences. The pressure on the underside of the front wing is slightly higher on the rolled car, and the pressure on the top is slightly lower. The downforce at the rear is higher on the rolled Mercedes-Benz, yet very small. The change may come from the area by the rear suspension, see circles in *figure 49*. The blue dot on the left side is decreasing, but the blue dot on the right side is increasing more.

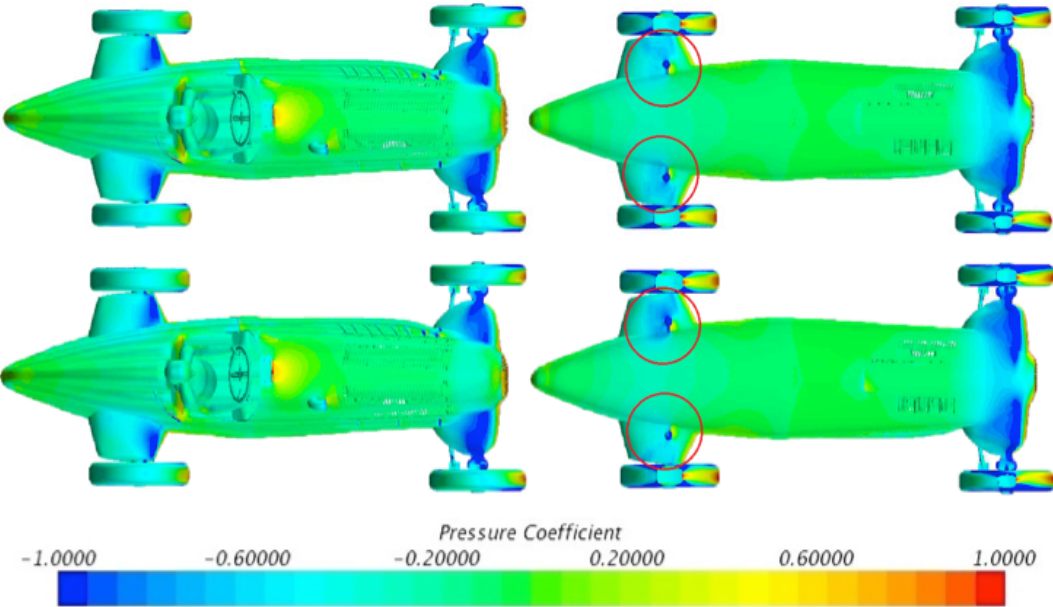


Figure 49 - Pressure coefficient on the Mercedes-Benz for 0° roll (top) and 2° roll (bottom).

8. Discussion

In this section the overall work from the methodology to the results is discussed and sources of errors are analysed.

8.1. Methodology and General Workflow

The method chosen for the project was a standard procedure for any CFD-process. This method is widely used and there is not any other method applied in similar procedures. For this reason and the simple fact that this is the logical way of performing simulations like ours, the choice was easily motivated. This section includes comments on the work along the way and from the different stages, which follows below.

8.1.1. Pre-Processing

At first it was not easy to understand how the CAD-models from the previous year were created. After some examination the group identified the problem areas and started modifying geometries according to the objectives with the models as originals. The changes were created without problems due to the good level of knowledge in CATIA V5 amongst the group members. The next phases of pre-processing, which was executed in ANSA and STAR-CCM+, was harder at first, mainly because the group lacked skill in these software's but after a four-day course in STAR-CCM+ the work began.

After a steep learning curve, these programmes started to feel more and more natural to the group and both cleaning geometries and modifying them for different simulations was done with ease. The numerous settings were set in line with examples from the course and in consultation with the supervisor. Some of these were to be changed several times when the solutions did not converge.

8.1.2. Solving

Just as the final stages of pre-processing, the solving was carried out in STAR-CCM+. The big struggle during this phase was to get the first simulation working, which took around one month. Different settings and geometries were changed and when this milestone was reached a schedule for further simulations was drawn.

In order to get all 24 simulations done in time, several computers were used and the results started falling out. Unfortunately, one of these simulations was not successful and therefore the results cannot be used.

8.1.3. Post-Processing

All the data from the solving was processed and scenes describing the forces, flow fields and pressure distribution etc. were created, which was also done in STAR-CCM+. The overall aim, to perform numerous simulations to fairly describe and compare the cars was now fulfilled and these are to be seen in the result and analysis section.

8.2. Sources of Errors

When CFD-simulations are done there are always sources of error that can affect the results. Our results are reasonable but might change if different choices had been made regarding CFD settings and CAD geometries.

8.2.1. Geometries

Throughout the project several possible sources of errors have been identified. Quite early in the project it was chosen to use the CMC-models. This decision was made for two reasons:

- The geometries in CATIA V5 from last year's bachelor thesis were based on the CMC-models, and we needed to use them as starting point to have enough time for simulations and post-processing.
- To check measurements on the models were easier than to find literature explaining it, and much easier than to measure on the real cars.

Therefore the authenticity of the models is crucial to be able to apply the conclusion to the real cars. As the work progressed two major differences between original cars and the models were discovered.

- The track, the width between the left and the right tyre, is not accurately depicted on the models. It is the model of the Auto-Union that is not true to the real car. According to literature the track of the front and rear wheels are the same in the type C. In the model this is not the case and this might have affected the results because it affects the projected area and flow in general. (Pritchard, 2008)
- Since the CMC-models are in scale 1:18, all the edges become sharper than on the actual cars. These sharp edges can in turn lead to separations that maybe would not be present on the actual cars. This can for example be seen on the radiator outlet on the side of the Auto Union.
- Another thing at the Auto-Union that is suspicious is the hole under the radiator. This vent is, in the model, placed in front of the radiator and therefore affects the pressure conditions on the radiator surface. At pictures in literature this hole cannot be seen and therefore it is more reasonable to believe that it should be placed downstream of the radiator (Pritchard, 2008).

If the track width changes, the total drag of the Auto Union is likely to change, but in what direction remains to be seen. If the hole underneath the radiator gets moved downstream, the air going through it will be at lower velocity and this in turn could lead to a change in separation with different drag and lift forces as a result.

Even when the models have been established as the basis of the work, more sources of errors remain. Simplifications in geometries have been made and some have been omitted. The ambition to make as authentic computer models as possible has determined the need to model parts at a certain level of detail. This could have been improved further if more time was available. All though, if this had been done, stricter requirements would apply on processes further down in the workflow.

One of the processes that would have been affected from such a change is the surface wrapper. To get a reasonable representation of the surface, the surface wrapper settings needed to be precise enough, but still not unnecessarily fine. If too fine; the computational power needed would be huge and this would also affect the volume mesh.

8.2.2. Computational Simplifications and Approximations

Generally a finer mesh could give a better resolution of the flow. If the aim was to analyse the cars at fine component level a higher resolution for the mesh would have been necessary. To get a better approximation at that level the boundary layer has to be fully resolved. Because of limitations in computational power the size of the generated meshes was not to exceed 10-15 million cells. At the chosen level of detail and in relation to the sought values this limitation was not majorly affecting the result.

All simulations were carried out at steady state flow, which represents the car moving at a constant speed. To obtain more realistic simulations, especially with pitch, yaw and roll, a transient setup would be a better choice. Transient simulations on the other hand require much more computer power and since we did not have access to that kind of computers this was not possible.

The choice of different discrete values of angles for the configurations may have affected the results and the overall trends of the analysis. To achieve a better and more comprehensive trend, the step size between the discrete values could be smaller and thereby get a more continuous picture of the whole sample range.

9. Conclusion

The conclusion that can be made is that most of the aerodynamical properties of the Mercedes-Benz are better than the Auto Union. The drag forces are for all different simulations significantly smaller on the Mercedes-Benz, and the lift forces are more evenly distributed. Since the Mercedes-Benz also has a front engine, the grip between the tyres and the ground will probably remain high even though there is just a small amount of downforce on the front axle. Unlike the Auto Union that had a very uneven distribution of lift forces with a lot of lift on the front axle and also a mid-engine resulting in nothing to keep the front down at high speeds. The Auto Union is likely harder to drive due to little grip between the front tyres and the ground.

The Auto Union had in all simulations a higher downforce on the rear axle than the Mercedes-Benz, this is most likely due to the rear wing on the Auto Union being located closer to the ground than the rear wing on the Mercedes-Benz. Since the Auto Union had a lot more engine power than the Mercedes-Benz, (Pritchard 2008), it could indicate that the engineers of the Auto Union knew that they needed a way to get the power through the wheels and into the ground. The best way to achieve this was with a mid-engine and with a wing generating a lot of downforce. The rear wing on the Auto Union looks like it is placed at its location for the purpose of generating downforce while the wings on the Mercedes-Benz are placed where they are to cover up the suspension and generate less drag. But if the engineers of the Auto Union truly understood downforce, they would have had an angle of attack on their rear wing.

To summarize; our simulations based the CMC-models show that the Mercedes-Benz is the better car in an aerodynamic perspective. But the Auto Union would probably run faster because of the high power and rear downforce and this could potentially lead to more wins.

9.1. Recommendations for Future Work

In this thesis there have been delimitations that when taken into consideration may lead to a different result. To truly understand the aerodynamic properties of the Silver Arrows some of these delimitations might need to be lifted.

In our simulations, the engine of both cars have a very similar exterior compared to the real cars, this simulates the flow around the engines very well. But since we do not take the internal airflow and thermodynamic properties of the engines into consideration the total drag caused by the engines has not really been analysed.

The changes in pitch and roll are effects caused by transient events. To really understand how the Auto Union and the Mercedes-Benz behave under cornering, braking and acceleration, transient simulations need to be done.

Both these tasks are important aspects of race car aerodynamics that we have not had the time or the knowledge to undertake. As said before, to really understand which one of the Silver Arrow race cars is better, this needs to be taken into consideration.

10. Bibliography

1. Barnard, R. H. (2010) *Road Vehicle Aerodynamic Design, 3rd Revised edition*, St Albans: Mechaero Publishing.
2. Prof. Dr. Bulut, Hüsamettin. (2006) *Reading texts for Mechanical Engineering*. ŞANLIURFA: Harran Üniversitesi Mühendislik Fakültesi.
3. David, D. (1999). *Grand Prix History*. Retrieved 2014-01-25 from <http://www.grandprixhistory.org/>
4. Fredrik Ejresjö, Björn Känge, David Kjellström, Mathias Lindbäck, Stefan Lundell, Markus Mybeck. (2013) *A CFD-Analysis and Aerodynamic Comparison of Two Silver Arrows*. Gothenburg: Chalmers University of Technology.
5. Eymard, Robert; Gallouët, Thierry; Herbin, Raphaële. (2000) *Finite Volume Methods, Handbook of numerical analysis, Vol. VII, Handbook Numerical Analysis, VII*. North-Holland, Amsterdam.
6. *Fluent 6.3 User's Guide*. (2006), New York: Fluent Inc.
7. Jerhamre, A. (2001) *On General Knowledge of Heat Exchangers*, Volvo Cars Internal Report Computational Fluid Dynamics, Gothenburg, Sweden.
8. Katz, Joseph. (1995) *Race Car Aerodynamics*. Cambridge: Bentley Publishers.
9. Dr. Maity, Subhendu. (2011) *Reynolds Stress Anisotropy Based Turbulent Eddy Viscosity Model Applied to Numerical Ocean Models*. Kharagpur: Indian Institute of Technology.
10. McDonough, James M. (2007) *Lectures in Computational Fluid Dynamics of incompressible flow*. Kentucky: University of Kentucky.
11. Pope, Stephen B. 2000. *Turbulent Flow*. Cambridge: Cambridge University Press.
12. Pritchard, Anthony. 2008. *Silver arrows in camera, 1934-39*. Sparkford: Haynes Publishing.
13. White, Frank M. 2011. *Fluid Mechanics. 7th Edition with SI units*. New York: McGraw-Hill Higher Education.
14. Wilcox, David C. 1994. *Turbulence modeling for CFD*. Palm Drive, La Cañada: DCW Industries, Inc.

12. Figure References

- Cover Page Warter, Stefan. (2011) *Audi tradition Calender*. www.autorevolution.com Retrieved 2014-05-27.
- Figure 1, Johan Bondesson, Henrik Forsting, Tim Gynning Olofsson, Gabriella Hjält, Gustav Markström, Erik Sjösvärd. (2014)
- Figure 2-5, Pritchard. (2008)
- Figure 6-7, Johan Bondesson, Henrik Forsting, Tim Gynning Olofsson, Gabriella Hjält, Gustav Markström, Erik Sjösvärd. (2014)
- Figure 8 left: Lothar Spurze. (1980), <http://en.wikipedia.org/wiki/File:AutoUnion16Zyl.jpg> Retrieved 2014-05-16
- Johan Bondesson, Henrik Forsting, Tim Gynning Olofsson, Gabriella Hjält, Gustav Markström, Erik Sjösvärd. (2014)
- Right, Fredrik Ejresjö, Björn Kange, David Kjellström, Mathias Lindbäck, Stefan Lundell, Markus Mybeck. (2013)
- Figure 9, Johan Bondesson, Henrik Forsting, Tim Gynning Olofsson, Gabriella Hjält, Gustav Markström, Erik Sjösvärd. (2014)
- Figure 10 left: Morio. (2013) http://commons.wikimedia.org/wiki/File:Mercedes-Benz_M25E_engine_Mercedes-Benz_Museum.jpg, Retrieved 2014-05-16
- Middle. Johan Bondesson, Henrik Forsting, Tim Gynning Olofsson, Gabriella Hjält, Gustav Markström, Erik Sjösvärd. (2014)
- Right, Fredrik Ejresjö, Björn Kange, David Kjellström, Mathias Lindbäck, Stefan Lundell, Markus Mybeck. (2013)
- Figure 11-49 Johan Bondesson, Henrik Forsting, Tim Gynning Olofsson, Gabriella Hjält, Gustav Markström, Erik Sjösvärd. (2014)

Appendix A

In this appendix the different surfaces included in each PID is presented.

PID name	Colour in figure 8
Exterior_Body_3	The external surface of the vehicle excluded the external parts
External_Parts_2	The steering wheel The side mirror The air intake The wing nuts The exhaust manifold The exhaust pipe The hooks for the engine lid The windshield
Front_Wheels_2	The front wheels
Gubbe_3	The driver
Helmet_2	The driver helmet and goggles
Interior_3_	The driver seat
Interior_Body_3	Interior surface of the vehicle
Radiator_Outlet	The radiator outlet
Radiator_Sides	The sides of the radiator
Radiator_inlet_2	The radiator inlet
Rear_Wheels_2	The rear wheels
Suspension_Front_2	The suspensions for the front wheels
Suspension_Rear_2	The suspensions for the rear wheels.
Vents_1	The vents
Wing_2	The wing at the rear of the vehicle.

Appendix B

In this appendix the whole CAD-models of the two Silver Arrow race cars can be seen.

Mercedes-Benz W25:



Auto Union Type C:

